NEUROSCIENCE

Perturbed cell fate decision by schizophrenia-associated AS3MT[d2d3] isoform during corticogenesis

Seunghyun Kim[1]†, Youngsik Woo[1]†, Dahun Um[1]†, Inseop Chun[1]†, Su-Jin Noh[1]†, Hyeon Ah Ji[1], Namyoung Jung[1], Bon Seong Goo[1], Jin Yeong Yoo[1], Dong Jin Mun[1], Tran Diem Nghi[1], Truong Thi My Nhung[1], Seung Hyeon Han[1], Su Been Lee[1], Wonhyeok Lee[1], Jonghyeok Yun[1], Ki Hurn So[1], Dae-Kyum Kim[2,3], Hyunsoo Jang[4], Yeongjun Suh[1], Jong-Cheol Rah[5], Seung Tae Baek[1,6], Ki-Jun Yoon[4], Min-Sung Kim[1,6]*, Tae-Kyung Kim[1,6]*, Sang Ki Park[1,6]*

The neurodevelopmental theory of schizophrenia emphasizes early brain development in its etiology. Genome-wide association studies have linked schizophrenia to genetic variations of *AS3MT* (arsenite methyltransferase) gene, particularly the increased expression of AS3MT[d2d3] isoform. To investigate the biological basis of this association with schizophrenia pathophysiology, we established a transgenic mouse model (AS3MT[d2d3]-Tg) ectopically expressing AS3MT[d2d3] at the cortical neural stem cells. AS3MT[d2d3]-Tg mice exhibited enlarged ventricles and deficits in sensorimotor gating and sociability. Single-cell and single-nucleus RNA sequencing analyses of AS3MT[d2d3]-Tg brains revealed cell fate imbalances and altered excitatory neuron composition. AS3MT[d2d3] localized to centrosome, disrupting mitotic spindle orientation and differentiation in developing neocortex and organoids, in part through NPM1 (Nucleophosmin 1). The structural analysis identified that hydrophobic residues exposed in AS3MT[d2d3] are critical for its pathogenic function. Therefore, our findings may help to explain the early pathological features of schizophrenia.

INTRODUCTION

Schizophrenia (SZ) is a psychiatric disorder with neurodevelopmental features that affects approximately 1% of the global population (*1*). Individuals with SZ exhibit impaired cognition, emotion, and social interaction, often accompanied by structural differences in the brain, such as ventricular enlargement (*2*, *3*). These structural changes suggest that impaired brain development may contribute to the behavioral and cognitive deficits seen in SZ (*4*). However, the specific developmental processes and underlying molecular mechanisms that lead to pathogenic defects remain unclear.

Multiple SZ genome-wide association studies (GWAS) have confirmed *AS3MT* (arsenite methyltransferase) as a key genetic risk factor (*5*, *6*). A subsequent study identified AS3MT[d2d3], an isoform of AS3MT lacking exons 2 and 3 encoding the first 102 amino acid residues due to alternative splicing prompted by a disease-associated single-nucleotide polymorphism (*7*). AS3MT[d2d3] expression is higher in the brain than in other tissues and is elevated in individuals with SZ (*7*). Although AS3MT[d2d3] lacks arsenite methyltransferase activity and is up-regulated during human stem cell differentiation toward neuronal fates (*7*), the specific roles in the developing brain have not been explored.

Proper regulation of the mitotic spindle during neurodevelopment is critical for chromosome segregation and cell fate determination (*8*). The orientation of the mitotic spindle is tightly controlled by astral microtubules from the centrosome (*9*). During early neurodevelopment, this process determines whether a neural progenitor undergoes symmetric or asymmetric division, ultimately deciding whether the progenitor will proceed to proliferation or differentiation pathways (*10*–*12*). Disruption of these balanced fate decisions can lead to neurodevelopmental disorders such as microcephaly and autism spectrum disorder (*12*, *13*).

In this study, we hypothesized that AS3MT[d2d3], independent of its enzyme activity, disrupts the early stage of neurodevelopment, contributing to the distortion of the neurodevelopmental process linked to SZ. To this end, we used a transgenic mouse model ectopically expressing AS3MT[d2d3] and investigated the potential link of AS3MT[d2d3] in neurodevelopment and associated SZ pathobiology. Our results showed that ectopic expression of AS3MT[d2d3] during early brain development perturbs critical processes that alter brain structure and mouse behavior. We also observed a characteristic centrosomal localization of AS3MT[d2d3], ultimately disrupting mitotic spindle orientation and cell fate balance. These findings emphasize the unexpected developmental function of AS3MT[d2d3] isoform linked to the pathology of SZ.

[1]Department of Life Sciences, Pohang University of Science and Technology, Pohang 37673, Republic of Korea. [2]Division of Thoracic and Upper Gastrointestinal Surgery, Department of Surgery, Faculty of Medicine and Health Sciences, McGill University, Montreal, Quebec H3G 1A4, Canada. [3]Cancer Research Program, Research Institute of McGill University Health Centre, Montreal, Quebec H4A 3J1, Canada. [4]Department of Biological Sciences, Korea Advanced Institute of Science and Technology, Daejon 34141, Republic of Korea. [5]Korea Brain Research Institute, Daegu 41062, Republic of Korea. [6]Institute for Convergence Research and Education in Advanced Technology, Yonsei University, Seoul 03772, Republic of Korea.
*Corresponding author. Email: ms.kim@postech.ac.kr (M.-S.K.); tkkim@postech.ac.kr (T.-K.K.); skpark@postech.ac.kr (S.K.P.)
†These authors contributed equally to this work.

RESULTS

AS3MT[d2d3]-Tg mice display ventricle enlargement

AS3MT[d2d3] exhibits increased expression in the SZ patient group, with up-regulation beginning at the neuronal fate determination stage (*7*). Building on these previous findings, we sought to determine whether AS3MT[d2d3] expression could be directly detected in neural progenitor cells (NPCs). We used the *AS3MT* E1E4 probe

for in situ hybridization (ISH) to specifically detect endogenous AS3MT^{d2d3} transcripts (*14*), along with the *AS3MT* E2E3 probe for AS3MT^{full}, and *SOX2* or *TUBB3* probes as cell type–specific markers on sections from 42-day human forebrain organoids (hFOs). We observed significantly higher AS3MT^{d2d3} expression in SOX2$^+$ NPCs compared to TUBB3$^+$ immature neurons (fig. S1, A and B). In contrast, AS3MT^{full} expression did not show a significant difference between SOX2$^+$ NPCs and TUBB3$^+$ immature neurons (fig. S1, C and D).

To replicate the cortical development modulated by AS3MT^{d2d3}, we established a transgenic mouse model using AS3MT^{d2d3} conditional overexpression. For this, the 1 to 306–base pair deleted form of mouse *As3mt* cDNA was inserted into a floxed "stop" cassette with the robust CAG promoter and knocked-in to the *Rosa26* locus (Fig. 1A). The mice were crossed with *Emx1*-Cre mice to ensure the expression of AS3MT^{d2d3} during the early stages of brain development. Expression of AS3MT^{d2d3} was confirmed by mCherry reporter fluorescence and Western blot analysis against AS3MT^{d2d3} in the forebrain of E14.5 AS3MT^{d2d3}-Tg (AS3MT^{d2d3};*Emx1*-Cre$^+$) mice (Fig. 1, B and C).

SZ is associated with observable variations in brain structure, such as ventricular enlargement (*2*, *15*). In this line, we analyzed the brains from postnatal day 60 (P60) AS3MT^{d2d3}-Tg mice. No significant alterations in the overall brain width and length were observed between AS3MT^{d2d3}-Tg (AS3MT^{d2d3};*Emx1*-Cre$^+$) and control (*Emx1*-Cre or AS3MT^{d2d3};*Emx1*-Cre$^-$) mice (Fig. 1, D to F). However, brain sections from adult AS3MT^{d2d3}-Tg mice showed an increased size in the lateral ventricles without significant change in the cerebral cortex (Fig. 1, G to I). We also used magnetic resonance imaging (MRI) on live mice for volumetric analysis of the brain structure (Fig. 1, J to M). The findings corroborated an augmented lateral ventricle size in the AS3MT^{d2d3}-Tg mice, while a significant difference in cortical volume was not detectable (Fig. 1, L and M).

AS3MT^{d2d3}-Tg mice exhibit SZ-associated behavioral deficits

To investigate whether the AS3MT^{d2d3}-Tg (AS3MT^{d2d3};*Emx1*-Cre$^+$) mice exhibit SZ-related behavioral deficits, we examined 10- to 12-week-old mice across a range of behaviors commonly linked to SZ, such as defective somatosensory gating, cognitive dysfunction, social withdrawal, and decreased emotional expression (*3*, *16*, *17*). In the prepulse inhibition (PPI) test, AS3MT^{d2d3}-Tg mice displayed reduced inhibition in response to a prepulse, indicating impaired sensory gating, while their startle response remained intact (Fig. 2, A and B). Cognitive function was evaluated using the Y-maze test, where no significant differences in spontaneous alternations were observed between AS3MT^{d2d3}-Tg and control mice, suggesting no notable deficits in working memory (Fig. 2C). Social behavior, a key domain affected in SZ, was assessed using the three-chamber social interaction test. AS3MT^{d2d3}-Tg mice exhibited altered social behavior, showing no preference for interacting with a stranger mouse, a hallmark of social impairment (Fig. 2, D to F). Furthermore, the time spent sniffing the stranger mouse was significantly reduced in AS3MT^{d2d3}-Tg mice, indicating decreased social engagement (Fig. 2G). This social deficit was further supported by lower nest-building scores, reflecting impaired social and motivational behaviors (Fig. 2, H and I). Despite these social and sensory gating abnormalities, AS3MT^{d2d3}-Tg mice did not exhibit anxiety-like behaviors in the open-field and elevated plus maze tests, as their performance in these assays was comparable to that of control mice (Fig. 2, J to M). These findings suggest that AS3MT^{d2d3} overexpression is associated with abnormal sensory gating and social behaviors, including reduced social interaction and motivation, which parallel the cognitive dysfunction, social withdrawal, and emotional blunting seen in patients with SZ.

AS3MT^{d2d3}-Tg mouse brain harbors altered excitatory neuron composition

To investigate the potential causes of the SZ-like phenotypes observed in AS3MT^{d2d3}-Tg mice, we analyzed the proportions of different cell types in the adult cerebral cortex of AS3MT^{d2d3}-Tg mice (AS3MT^{d2d3}; *Emx1*-Cre$^+$) and their control littermates (AS3MT^{d2d3};*Emx1*-Cre$^-$). We performed single-nucleus RNA sequencing (snRNA-seq) to characterize the cellular composition and transcriptional landscapes in the P60 cerebral cortex (Fig. 3A), analyzing 42,329 nuclei from control mice and 36,300 nuclei from AS3MT^{d2d3}-Tg mice using the 10× Genomics platform. The snRNA-seq data were of high quality and highly reproducible across replicates (fig. S2, A to C). Clustering and annotation analyses revealed distinct alterations particularly in clusters representing excitatory neurons in the AS3MT^{d2d3}-Tg, specifically clusters 20 and 28 (Fig. 3, B and C, and fig. S2, D and F). A detailed analysis of excitatory neurons across cortical layers, layer 2/3 marked by *Cux2* and *Calb1*, layer 5 marked by *Etv1*, and layer 6 marked by *Syt6* and *Foxp2*, showed significant reductions in neuron populations especially within layer 2/3 (cluster 11 and 22) in AS3MT^{d2d3}-Tg mice (Fig. 3, D and E, and fig. S2, E and G).

The clusters that showed a proportional reduction exhibited high expression level of *Tshz2* (Teashirt zinc finger homeobox 2), with *Tshz2* being the most highly expressed gene in clusters 11 and 22 (Fig. 3, F and G, and fig. S3A). The *Tshz2* is known to be expressed across all layers in the anterior cingulate cortex (ACC) and retrosplenial (RSP) areas, with relatively enriched expression at layer 5 in other cortical regions (*18*). Analysis of ISH data from the Allen Brain Atlas corroborated this (*19*), confirming *Tshz2* expression across all layers particularly in the ACC and RSP (fig. S3B). Thus, the observed reduction in the Tshz2$^+$ layer 2/3 neurons in the AS3MT^{d2d3}-Tg mice is likely concentrated in the ACC and RSP.

Immunohistochemistry (IHC) using Tshz2 antibody in the ACC sections further validated these findings, showing a significant reduction in Tshz2$^+$NeuN$^+$ cells within NeuN$^+$ cells, specifically in layer 2/3 (Fig. 3, H to J). This conclusion was supported by an analysis of Tshz2 expression and layer marker genes (fig. S3, C and D). Furthermore, staining for general markers, such as Cux1, Ctip2, Satb2, and γ-aminobutyric acid (GABA), in the ACC and somatosensory regions revealed a significant reduction in Cux1$^+$NeuN$^+$ cells within NeuN$^+$ cells in the ACC (fig. S4, A to L). Neuronal density analysis in Cux1$^+$ or Ctip2$^+$ regions also confirmed the decreased population of layer 2/3 neurons in AS3MT^{d2d3}-Tg mice (fig. S5, A to C).

AS3MT^{d2d3} expression perturbs NSC fate

Abnormal neurogenesis is associated with alteration in the cortical neuron population (*12*). We investigated whether neurogenesis and differentiation were affected in AS3MT^{d2d3}-Tg mice. To assess cell composition and differentiation within the embryonic cerebral cortex, we performed single-cell RNA sequencing (scRNA-seq) using the 10x Genomics platform. We analyzed 15,128 cells from embryonic day 15.15 (E15.5) cerebral cortex of control littermate mice (AS3MT^{d2d3};*Emx1*-Cre$^-$) and 15,118 cells from E15.5 cerebral cortex of AS3MT^{d2d3}-Tg mice (AS3MT^{d2d3};*Emx1*-Cre$^+$) (Fig. 4A). The scRNA-seq data were of high quality and showed strong reproducibility
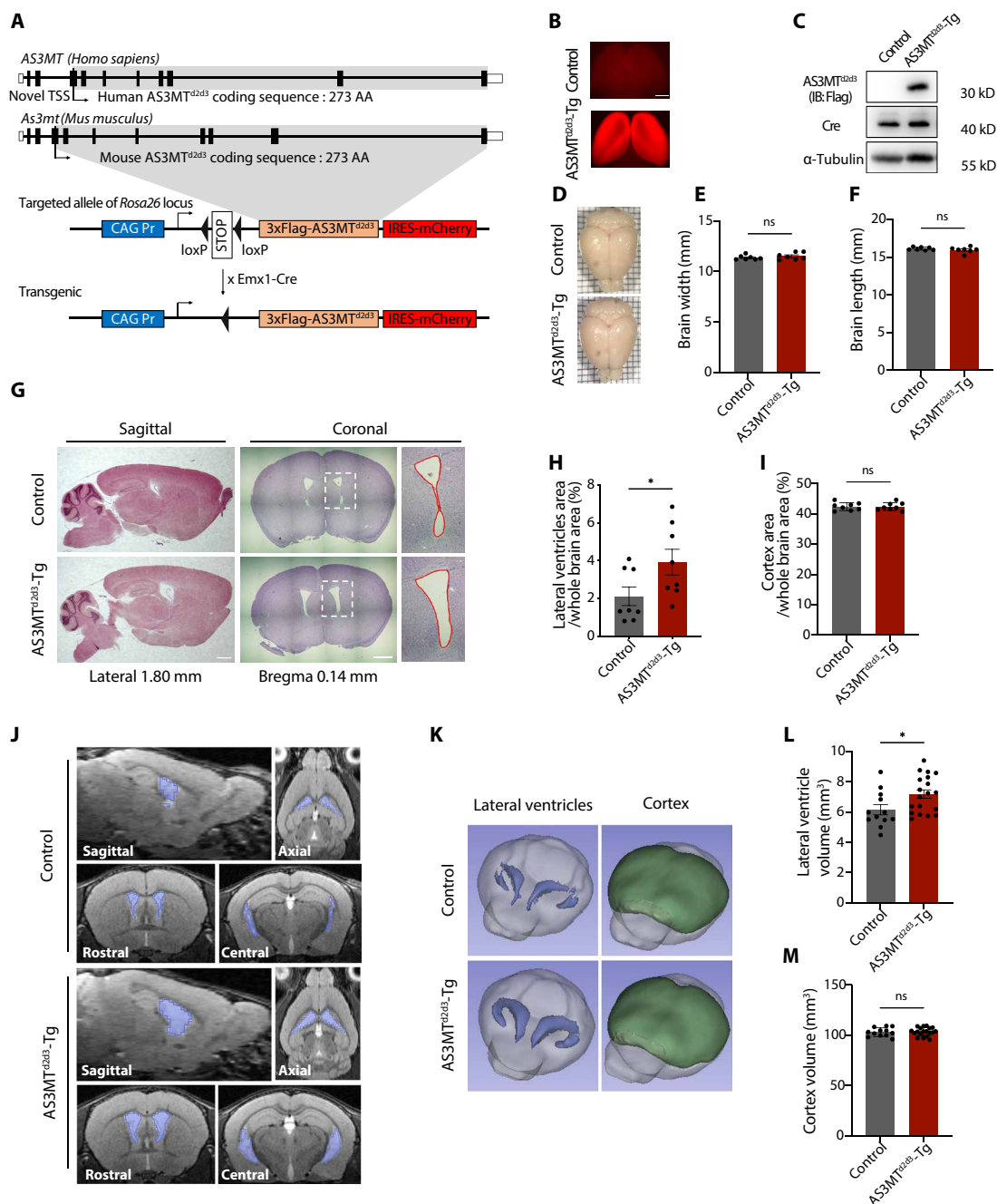
Fig. 1. AS3MT^d2d3-Tg mice display ventricle enlargement. (**A**) Schematic diagrams of the *AS3MT* and *As3mt* genomic region and the Cre-dependent mouse AS3MT^d2d3 and reporter gene expression construct at the *Rosa26* locus in the transgenic mice. Gray areas represent AS3MT^d2d3 coding regions. (**B**) Fluorescence images of E14.5 embryonic cortex from control and AS3MT^d2d3-Tg mouse. (**C**) Western blot from control and AS3MT^d2d3-Tg embryonic brains. (**D**) P60 brains from control and AS3MT^d2d3-Tg mouse on the 1-mm^2 paper. (**E** and **F**) Quantification of brain width and length (Control, $n = 7$; AS3MT^d2d3-Tg, $n = 7$). (**G**) Hematoxylin and eosin staining from littermate control and AS3MT^d2d3-Tg mouse brains at the coordinate lateral (1.80 mm) and (bregma 0.14 mm). (**H** and **I**) Quantification of the percentage of lateral ventricle or cortex area at the coronal section (Control, $n = 8$; AS3MT^d2d3-Tg, $n = 8$). (**J**) Slices from littermate control and AS3MT^d2d3-Tg mice brain MRIs. (**K**) Volumetric views of the lateral ventricles and cortex. (**L** and **M**) Quantification of lateral ventricle and cortex volume (Control, $n = 12$; AS3MT^d2d3-Tg, $n = 19$). Scale bars, (B) 500 μm and (B) 1 mm. Bar graphs show means ± SEM. Statistical significance is defined by unpaired two-tailed t tests; $*P < 0.05$. TSS, translation start site; AA, amino acids; ns, not significant.
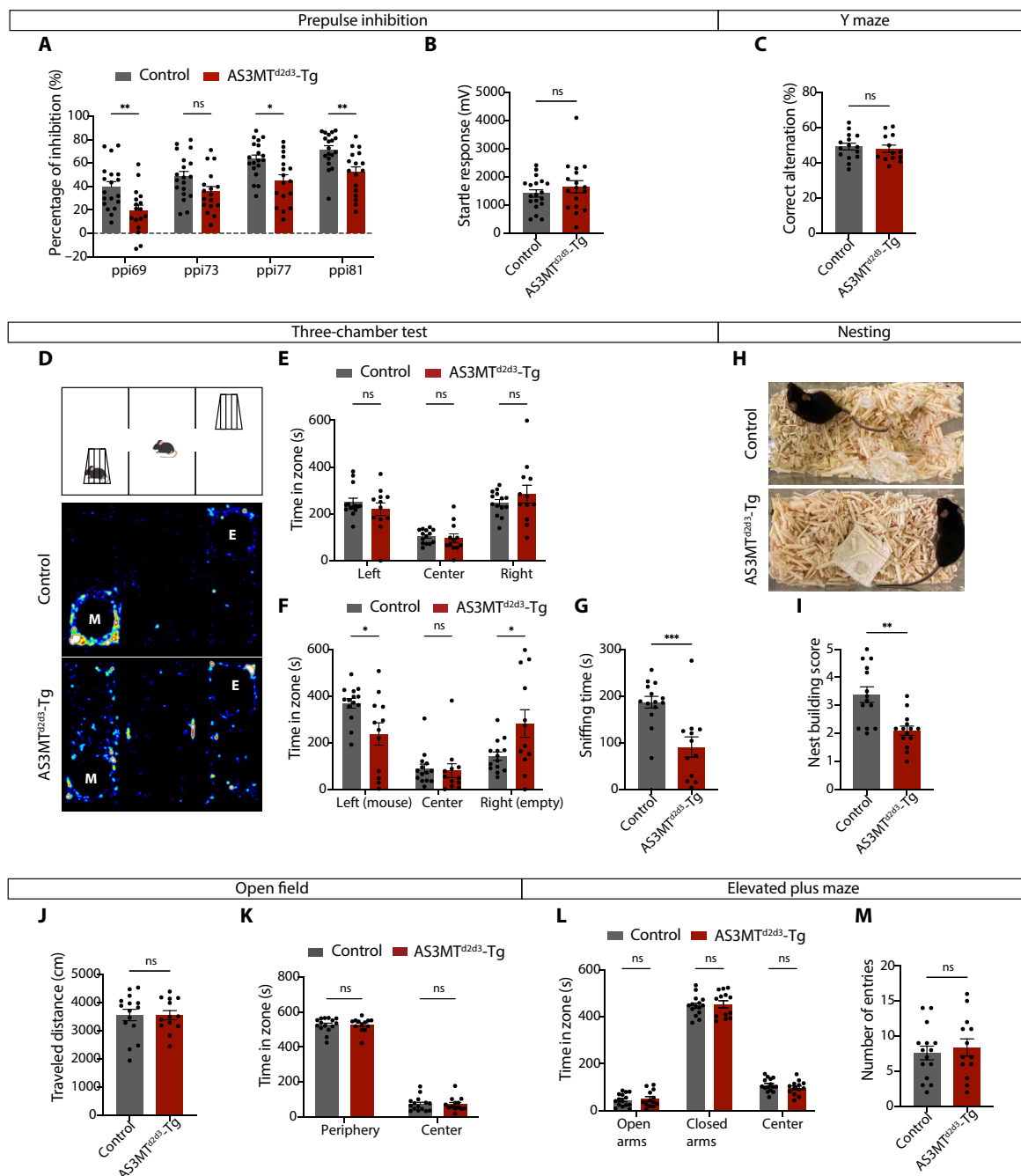
Fig. 2. AS3MT^d2d3-Tg mice exhibit SZ-associated behavioral deficits. (**A**) Quantification of the percentage of PPI to a prepulse of 69, 73, 77, and 81 dB (Control, $n = 19$; AS3MT^d2d3-Tg, $n = 17$). (**B**) Quantification of the startle response (Control, $n = 19$; AS3MT^d2d3-Tg, $n = 17$). (**C**) Quantification of the percentage of correct alternation in the Y-maze test (Control, $n = 15$; AS3MT^d2d3-Tg, $n = 13$). (**D**) Map of the chambers (left with mice in a cage "M," center, and right with an empty cage "E") and heatmaps during the test period. (**E**) Quantification of time spent during the habituation period (Control, $n = 14$; AS3MT^d2d3-Tg, $n = 12$). (**F**) Quantification of time spent during the test period (Control, $n = 14$; AS3MT^d2d3-Tg, $n = 12$). (**G**) Quantification of sniffing time spent interacting with a mouse (Control, $n = 14$; AS3MT^d2d3-Tg, $n = 12$). (**H**) Images of the nesting behavior. (**I**) Quantification of the nest building score (Control, $n = 14$; AS3MT^d2d3-Tg, $n = 14$). (**J**) Quantification of traveled distance (Control, $n = 15$; AS3MT^d2d3-Tg, $n = 13$). (**K**) Quantification of time spent in the center and periphery (Control, $n = 15$; AS3MT^d2d3-Tg, $n = 13$). (**L**) Quantification of time spent in open arms, closed arms, and center (Control, $n = 15$; AS3MT^d2d3-Tg, $n = 13$). (**M**) Quantification of the number of entries (Control, $n = 15$; AS3MT^d2d3-Tg, $n = 13$). Bar graphs show the means ± SEM. Statistical significance is defined by unpaired two-tailed t tests for two groups except nesting behavior (Mann Whitney test) and two-way analysis of variance (ANOVA) with Bonferroni's post hoc test for comparisons among multiple groups; *$P < 0.05$; **$P < 0.01$; ***$P < 0.001$.
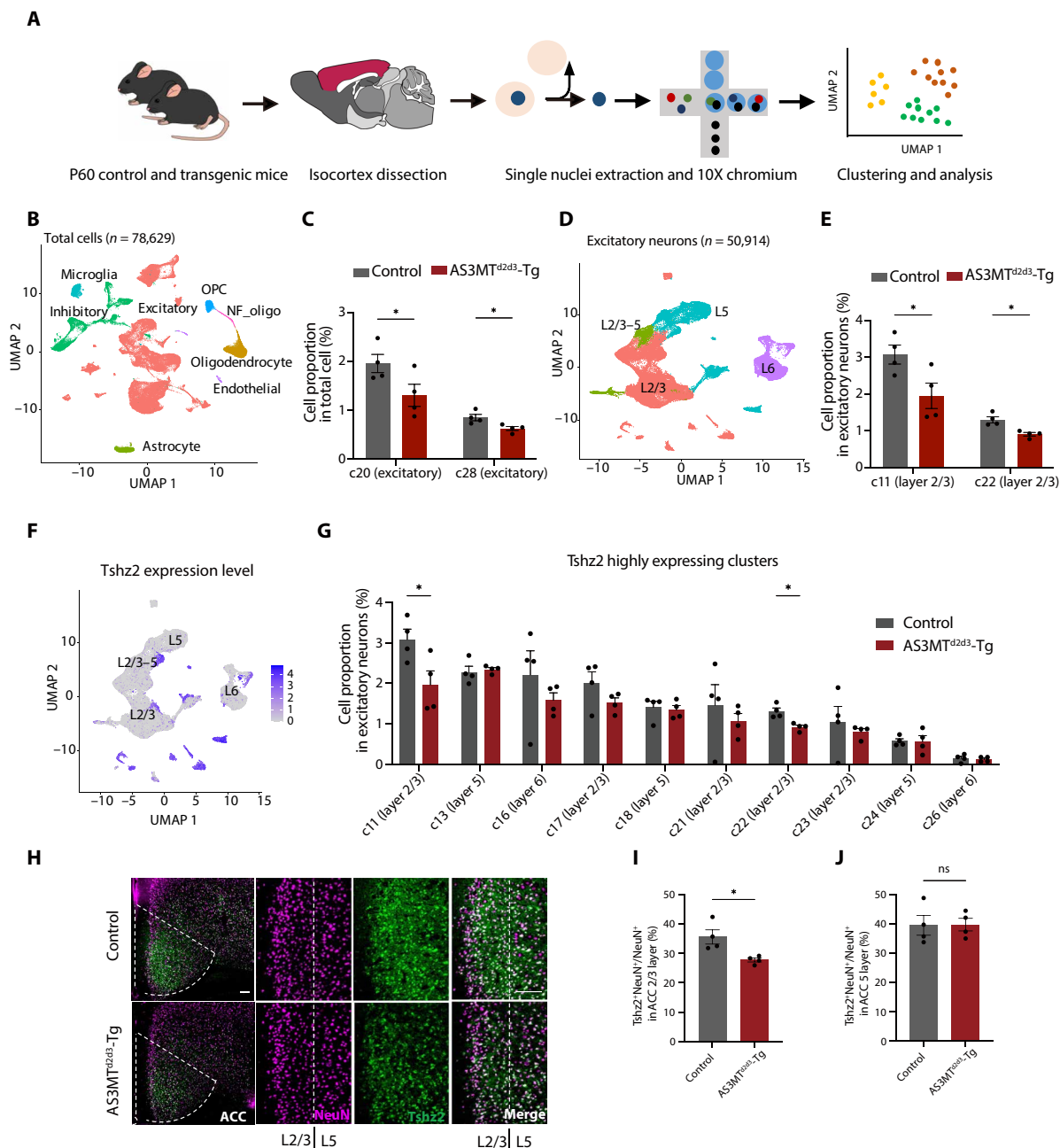
Fig. 3. AS3MT^{d2d3}-Tg mice brain harbors altered excitatory neuron composition. (**A**) Overview of the experimental approach. Nuclei of cortical cells were isolated from P60 littermate control or AS3MT^{d2d3}-Tg mice across four biological replicates. (**B**) Uniform Manifold Approximation and Projection (UMAP) embedding of integrated snRNA-seq cell type annotation from total cells ($n = 78,629$). (**C**) Statistically significant clusters from proportion analysis of total cells (c20 and c28). (**D**) UMAP embedding of integrated snRNA-seq cell type annotation from excitatory neurons ($n = 50,914$). (**E**) Statistically significant clusters from proportion analysis of excitatory neurons (c11 and c22). (**F**) Tshz2 expression level in UMAP plot from excitatory neuron. (**G**) Tshz2-high expression clusters from proportion analysis of excitatory neurons. (**H**) Brain sections stained with antibodies against Tshz2 and NeuN in control and AS3MT^{d2d3}-Tg mice. The dotted line indicates the ACC (left) and the layer boundary (right). (**I** and **J**) Quantification of the Tshz2$^+$NeuN$^+$ cells among NeuN$^+$ cells in layer 2/3 or layer 5 (Control, $n = 4$; AS3MT^{d2d3}-Tg, $n = 4$). Scale bars, 100 μm. Bar graphs show the means ± SEM. Statistical significance is defined by moderate t test for snRNA-seq analysis and unpaired two-tailed t tests for immunostaining analysis; *$P < 0.05$. OPC, oligodendrocyte progenitor cell; NF_oligo, newly formed oligodendrocyte; ACC, anterior cingulate cortex.
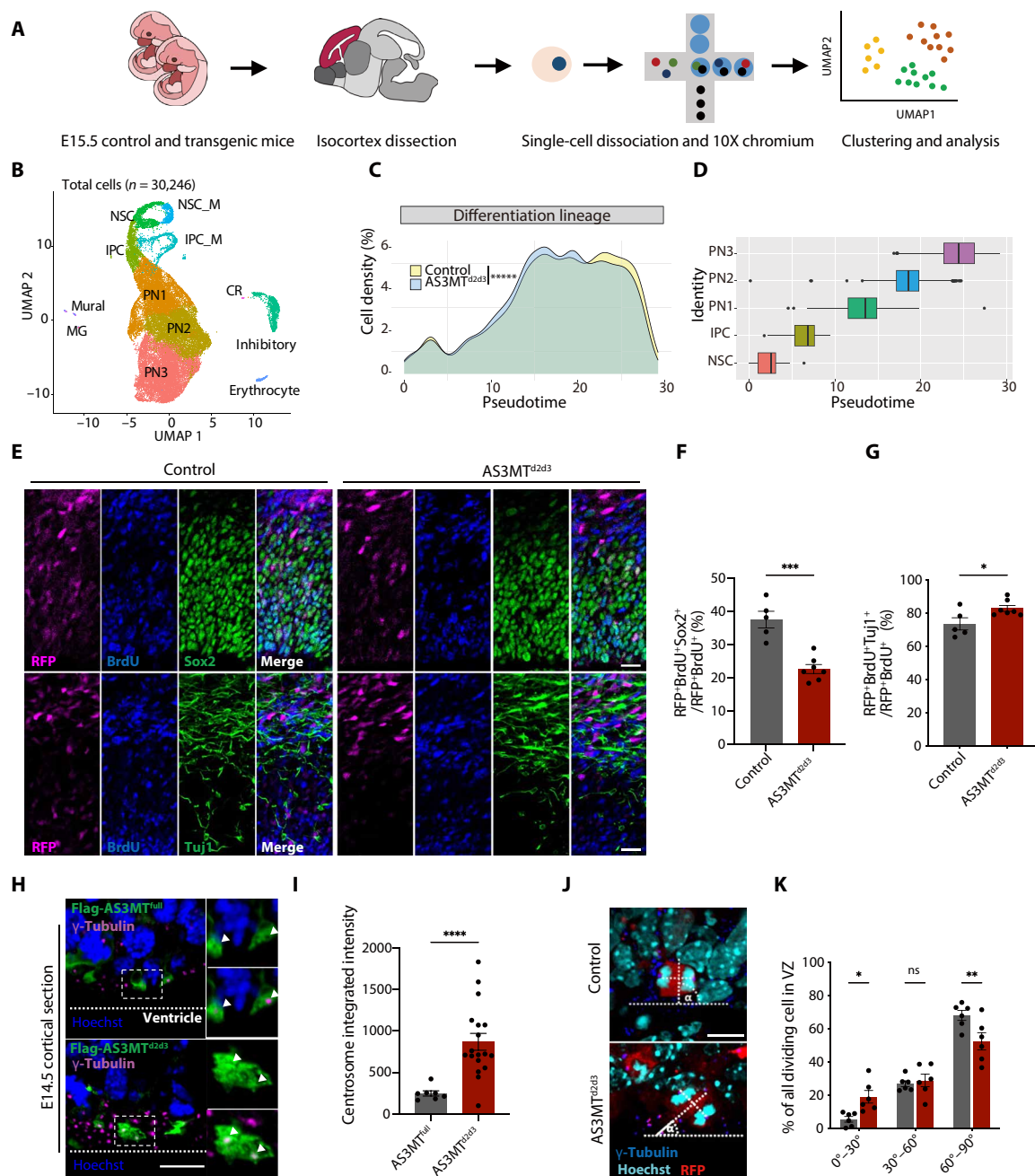
Fig. 4. AS3MT^d2d3 expression perturbs NSC fate and spindle orientation with evidence of centrosome localization. (**A**) Overview of the experimental approach. Cortical cells were isolated from E15.5 littermate control or AS3MT^d2d3-Tg mice across two biological replicates. (**B**) UMAP embedding of integrated scRNA-seq cell type annotation (n = 30,246). (**C** and **D**) Trajectory inference and pseudo-time analysis between control and AS3MT^d2d3-Tg. (**E**) E15.5 brain sections stained as indicated. in utero electroporation at E13.5 and BrdU injection at E14.5. (**F** and **G**) Quantification of the percentage of RFP⁺BrdU⁺Sox2⁺ or RFP⁺BrdU⁺Tuj1⁺ cells among the RFP⁺BrdU⁺ cells (Control, n = 5; AS3MT^d2d3, n = 7). (**H**) Subcellular localization of Flag-AS3MT^full or Flag-AS3MT^d2d3 in E14.5 brain sections, stained as indicated. (**I**) Quantification of the centrosome integrated intensity marked by γ-tubulin (AS3MT^full, n = 7; AS3MT^d2d3, n = 18). (**J**) E14.5 brain sections stained as indicated. in utero electroporation at E13.5. Dotted line indicates orientation of the sister chromatids (α). (**K**) Quantification of the percentage of cortical progenitors within each 30° interval (Control, n = 6; AS3MT^d2d3, n = 6). Scale bars, (E) 20 μm and [(H) and (J)] 10 μm. Bar graphs show the means ± SEM. Statistical significance is defined by unpaired two-tailed t tests for Sox2 and Tuj1 staining analysis, Welch's t test for centrosome staining analysis, Kolmogorov-Smirnov test for trajectory analysis, and two-way ANOVA with Bonferroni's post hoc test for comparisons among multiple groups; *P < 0.05; **P < 0.01; ***P < 0.001; ****P < 0.0001; *****P < 0.00001. NSC, neural stem cell; NSC_M, NSC in mitosis; IPC, intermediate progenitor cell; IPC_M, IPC in mitosis; PN, projection neuron; MG, microglia; CR, Cajal-Retzius; VZ, ventricular zone.

across replicates (fig. S6, A and B). Clustering and annotation analysis demonstrated that most cell populations in both groups were seemingly indistinguishable (Fig. 4B and fig. S6C). To better understand neuronal development at this stage, we applied trajectory inference analysis (20), defining cell lineages from neural stem cells (NSCs) to intermediate progenitor cells (IPCs), followed by projection neuron (PN) stages (PN1, PN2, and PN3) (fig. S6, D and E). The trajectory plot revealed significant differences in the neuronal development path of the AS3MT^{d2d3}-Tg mice compared to controls (Fig. 4, C and D). Pseudotime analysis based on transcriptional profiles indicated that cells from AS3MT^{d2d3}-Tg mice displayed increased premature differentiation, particularly at the IPC, PN1, and PN2 stages. This was accompanied by a reduction in cell density at the NSC stage and at the later stage of neuronal development (PN3), suggesting that elevated AS3MT^{d2d3} expression in NPCs leads to changes in cell fate, resulting in premature depletion of the neural progenitor pool (Fig. 4, C and D).

To validate this observation, we performed in utero electroporation of E13.5 mouse embryos with a red fluorescent protein (RFP) marker and an AS3MT^{d2d3} expression construct. One day later, bromodeoxyuridine (BrdU) was injected intraperitoneally to track the fate of cycling progenitors. At E15.5, BrdU- and RFP-labeled cells were analyzed by IHC using progenitor (Sox2) and neuronal (Tuj1) markers (Fig. 4, E to G). Ectopic expression of AS3MT^{d2d3} led to a significant reduction in the pool of apical progenitors without reduction in the pool of intermediate progenitors (Fig. 4F fig. S7, A to D). Conversely, there was a notable increase in the population of differentiated neurons (Fig. 4G and fig. S7, E and F), indicating that the up-regulation of AS3MT^{d2d3} expression in NPC results in premature differentiation during neurogenesis.

We further examined the effect of AS3MT^{d2d3} in hFOs to confirm this human specific isoform in human system. We generated 7-week-old hFOs from H9 stem cell lines (fig. S8A) and injected the AS3MT^{d2d3} expression construct with an enhanced green fluorescent protein (EGFP) marker or control vector into the rosettes of hFOs to assess its impact on the NSC pool and differentiation. Sox2 was used as a ventricular zone (VZ)–like rosettes marker and Tuj1 as a cortical zone marker within hFOs. In the AS3MT^{d2d3} overexpressed hFOs, there was a significant decrease in Sox2$^+$GFP$^+$ cells among GFP$^+$ cells (fig. S8B) and a significant increase in the Tuj1$^+$GFP$^+$ cells among GFP$^+$ cells (fig. S8C). These findings collectively suggest that the ectopic expression of AS3MT^{d2d3} induces premature differentiation and depletion of the NSC pool during cortical development, deduced from the observation in mouse brain and hFOs.

AS3MT^{d2d3} localizes to the centrosome and promotes asymmetric division during embryonic neurogenesis

We examined the subcellular localization of AS3MT^{full} and AS3MT^{d2d3} in human embryonic kidney (HEK) 293FT cells to understand their roles in relevant cell fate determination. Notably, while Flag-AS3MT^{full} was predominantly distributed in the cytosol, Flag-AS3MT^{d2d3} exhibited a stronger signal at the centrosome (fig. S9, A and B). This finding was further supported by centrosome fractionation experiment in HEK293FT cells coexpressing AS3MT^{full} and AS3MT^{d2d3}, which demonstrated notable enrichment of AS3MT^{d2d3} in the γ-tubulin–positive centrosomal fractions (fig. S9C). In addition, in utero electroporation of E14.5 mouse brains confirmed the enriched centrosome localization of Flag-AS3MT^{d2d3} compared with Flag-AS3MT^{full} (Fig. 4, H and I).

During early cortical development, NSCs and IPCs in the VZ undergo divisions to produce postmitotic neurons that migrate radially to form successive cortical layers (21, 22). The centrosomal localization and increased expression of AS3MT^{d2d3} at the NSC stage prompted us to examine its role in mitosis. We analyzed mitotic spindle orientation in serine-55–phosphorylated vimentin (p-Vim)–positive NPCs at E14.5 by measuring the angle between the cleavage plane and VZ surface (Fig. 4J) (23). In AS3MT^{d2d3}-expressing cells, the mean mitotic spindle orientation showed a horizontal tilt (fig. S9D). Dividing progenitors were categorized into three groups based on the cleavage plane orientation relative to the apical surface: horizontal (0° to 30°), intermediate (30° to 60°), and vertical (60° to 90°). In the control embryos, most dividing cells displayed vertical cleavage planes, with fewer showing horizontal cleavage planes. In contrast, AS3MT^{d2d3}-expressing embryos displayed fewer vertical cleavage planes and increased horizontal cleavage planes (Fig. 4K and fig. S9D). Similar trends were observed in E12.5 control mice and AS3MT^{d2d3}-Tg mice (fig. S9, E to G), indicating that elevated AS3MT^{d2d3} expression in neural progenitors results in spindle misorientation and a higher frequency of asymmetric divisions with horizontal cleavage planes.

To further investigate the function of AS3MT^{d2d3}, we performed coimmunoprecipitation and mass spectrometry (co-IP/MS) on Flag-AS3MT^{d2d3} and Flag-AS3MT^{full} expressed in HEK293FT cells. The AS3MT^{d2d3} sample revealed a broader range of interactomes than AS3MT^{full}, including centrosome-associated proteins VIM and nucleophosmin 1 (NPM1) (fig. S10, A and B). To assess the functional relevance of these interactions, we conducted spindle orientation assays following the knockdown (KD) of NPM1 and VIM in vivo. The NPM1 KD, not VIM, induced defective spindle orientation, implying its functional link to AS3MT^{d2d3} in regulating mitotic spindle orientation (fig. S10, C to F, and table S1).

Given that NPM1 is known for its role in mitotic spindle regulation and microtubule nucleation (24, 25), we analyzed microtubule organization in mitotic cells expressing AS3MT^{d2d3}. We observed a significant reduction in both the number and length of microtubules extending from the centrosome to the plasma membrane (fig. S11, A to C). This astral microtubule defect suggested potential chromosome segregation errors during mitosis. AS3MT^{d2d3}-expressing cells displayed a higher frequency of abnormal chromosome distribution compared to controls (fig. S11, D and E). These findings indicate that AS3MT^{d2d3} not only localizes to the centrosome but also affects mitotic spindle dynamics and chromosome segregation.

We also investigated the potential link to known centrosome-associated proteins CDK5RAP2, WDR62, and ASPM, which have been implicated in spindle orientation regulation (26, 27). Given that *Cdk5rap2* mutant mice exhibit centrosome duplication defects and increased cell death, we conducted detailed analyses including abnormal spindle pole counting, cleaved Caspase-3 staining, and cell death–related gene expression profiling in scRNA-seq data (fig. S11, F and G, and fig. S12, A and B). In these analyses, no notable phenotypes were induced by AS3MT^{d2d3}. In addition, immunostaining for CDK5RAP2, WDR62, and ASPM in NPCs from hFOs revealed no significant changes in their centrosome localization upon the expression of AS3MT^{d2d3} (fig. S13, A to F).

We also explored the potential impact on later neurodevelopmental processes. We performed in utero electroporation at E15.5 followed by an analysis of neuronal migration at E18.5 and could not detect significant migration defects (fig. S14, A and B). In addition, analyses of cellular morphology during the E13.5 to E15.5

period showed no significant changes in the proportions of round, multipolar, or bipolar cells (fig. S14, C and D). Last, axon formation was examined from E14.5 to P6, and no significant differences in axon length or ipsilateral branching were observed (fig. S14, E to H). These results indicate that the impact of the enhanced AS3MT^{d2d3} expression is relatively specific to the initial stage of neurodevelopment.

Exposed hydrophobic residues of AS3MT^{d2d3} drive centrosome localization and spindle misorientation

Since AS3MT^{d2d3} is the N-terminal deletion form of AS3MT^{full}, we hypothesized that the protein structural difference resulting from the deletion might affect its molecular characteristics. We successfully determined the 2.65-Å–resolution crystal structure of human AS3MT^{full} (Fig. 5A and table S2). However, we encountered challenges in obtaining the crystal structure of AS3MT^{d2d3} due to heterogeneous protein peaks with homodimer size during size exclusion chromatography (Fig. 5B). To overcome this, we used a modeling algorithm to compare the structures of AS3MT^{full} and AS3MT^{d2d3}, revealing that the N-terminal deletion in AS3MT^{d2d3} exposes hydrophobic residues, including V129 and F131 (Fig. 5A). To assess the importance of these exposed residues for the molecular characteristics of AS3MT^{d2d3}, we introduced mutations that replaced the hydrophobic residues with hydrophilic ones (V129D and F131D). Size exclusion chromatography demonstrated that these hydrophilic substitutions eliminated homodimerization of AS3MT^{d2d3} (Fig. 5B). Furthermore, the centrosomal localization of AS3MT^{d2d3} was significantly reduced with these mutations (Fig. 5, C and D), suggesting that the exposed hydrophobic residues of AS3MT^{d2d3} are indeed critical for centrosomal localization.

To test the relevance of spindle orientation phenotype by using human AS3MT^{d2d3} V129D and F131D mutant, human organoids are a suitable platform (28–30). We can also investigate whether AS3MT^{d2d3} expression contributes to spindle dysregulation in NSCs of the human system. Six-week-old hFOs were generated from the cell lines doxycycline (dox)–dependently AS3MT^{d2d3}-expressing lines or AS3MT^{d2d3} V129D/F131D-expressing lines (fig. S15, A to C). Immunostaining was performed to analyze spindle orientation in mitotic NSCs, with anti–p-Vim antibody labeling used to identify mitotic NSCs. We measured the angle between the mitotic cleavage plane and the apical VZ surface, representing spindle orientation. Consistent with our findings in developing mouse brains, dox$^+$/AS3MT^{d2d3} hFOs displayed a significant disruption in the cleavage plane compared to dox$^-$/AS3MT^{d2d3} controls (Fig. 5, E and F, and fig. S15D). In contrast, AS3MT^{d2d3} V129D/F131D, which showed reduced centrosome localization, did not induce a significant disruption in the cleavage plane compared to dox$^-$/AS3MT^{d2d3} V129D/F131D controls (Fig. 5, G and H, and fig. S15E). These results indicate that centrosome localization of AS3MT^{d2d3}, driven by exposed hydrophobic residues, can affect proper spindle orientation during NSC dividing.

DISCUSSION

Although elevated expression of AS3MT^{d2d3} in individuals with SZ has been reported (7), the biological implication of this exaggerated expression remains unelucidated. In this study, we aimed to bridge the genetic findings linking increased AS3MT^{d2d3} expression to SZ risk by constructing a mouse model that encompasses two critical aspects: (i) ectopic expression of mouse form of AS3MT^{d2d3} and (ii) initiation of this expression from the early neurogenesis stage. First, we designed the ectopic expression of the mouse form of AS3MT^{d2d3}

to faithfully replicate the condition of patients with SZ within the mouse background. This approach aligns with the strategies used in other SZ model mice, such as truncated Disc1 (disrupted in schizophrenia 1) transgenic mice, which mimic patient-related phenotypes, and mouse models of elevated C4 expression, linking GWAS risk factors to cortical endophenotypes of SZ (31, 32). Second, considering the substantial increase in AS3MT^{d2d3} expression from the early neurogenesis stage in human stem cell models (7) and our ISH data in hFOs, we postulated that this developmental stage could represent a critical period for disease-relevant effects of excessive AS3MT^{d2d3} expression. Thus, the AS3MT^{d2d3} mice were bred with the *Emx1*-Cre mice to initiate the AS3MT^{d2d3} expression from the NSC, following other studies to investigate neurogenesis stages (33, 34). Consequently, our findings using this strategy underscore the importance of AS3MT^{d2d3} expression during neural development. The expression of mouse AS3MT^{d2d3} from the NSC stage in the AS3MT^{d2d3}-Tg mice was sufficient to induce changes in the brain structure and behavior phenotypes that parallel those observed in patients with SZ (2, 3, 15, 17). Furthermore, we validated the relevance of our mouse model by demonstrating that the expression of human AS3MT^{d2d3} from the NSC stage in hFOs recapitulated the key phenotypes observed in mouse AS3MT^{d2d3} phenotypes such as mitotic spindle orientation and NSC fate. These results emphasize the potential value of the AS3MT^{d2d3}-Tg mouse model for studying the SZ susceptibility associated with AS3MT^{d2d3} and provide insights into the molecular mechanisms underlying SZ.

Lateral ventricle enlargement is one of the objective markers in SZ, consistently observed in MRI studies of patients with SZ (2, 15, 35). This phenotypic manifestation is not limited to human subjects; it is also evident in SZ mouse models, such as the Nrg1 (neuregulin 1) overexpression mouse (36), which exhibits ventricle enlargement alongside disrupted neurogenesis (37). Ventricle enlargement is also widely recognized as a hallmark of neurogenesis dysregulation, supported by genetic knockout studies of *Dyrk1a*, *Sox2*, *Wdfy3*, and *Parp1* demonstrating defects in NSC proliferation or maintenance that lead to this ventricle phenotype (38–41). These consistent associations between perturbed neurogenesis and ventricle enlargement have prompted recent investigations into the role of NSCs in ventricular neuroepithelium in the context of abnormal prenatal neurogenesis and its impact on ventricle size (42). Notably, *TRIM71* (tripartite motif containing 71), the most frequently mutated gene in human congenital hydrocephalus, provides a prototypical example of NSC involvement in ventricle enlargement. In *TRIM71* knockout mice, premature neuronal differentiation at the expense of NSC expansion results in ventricle enlargement (43). Similarly, cerebral cortical organoids derived from iPSCs of a patient with SZ reveal early developmental defects in cortical neural progenitors, disrupting neuronal differentiation and reducing neurogenesis (44). In line with these findings, we observed that AS3MT^{d2d3}-Tg mice show ventricle enlargement concurrent with premature neuronal differentiation and a reduction in NSC population. Our results align with the growing body of evidence linking neurogenesis, ventricle enlargement, and SZ pathophysiology, emphasizing the relevance of AS3MT^{d2d3} in SZ and its potential contribution to the disorder's etiology.

Our study revealed aberrant social behavior and defective somatosensory gating in AS3MT^{d2d3}-Tg mice (3, 17). Our snRNA-seq analysis unveiled a significant reduction of Tshz2$^+$ population of layer 2/3 excitatory neurons in these mice, a finding further confirmed by immunostaining in the ACC. Notably, the abnormal layer composition
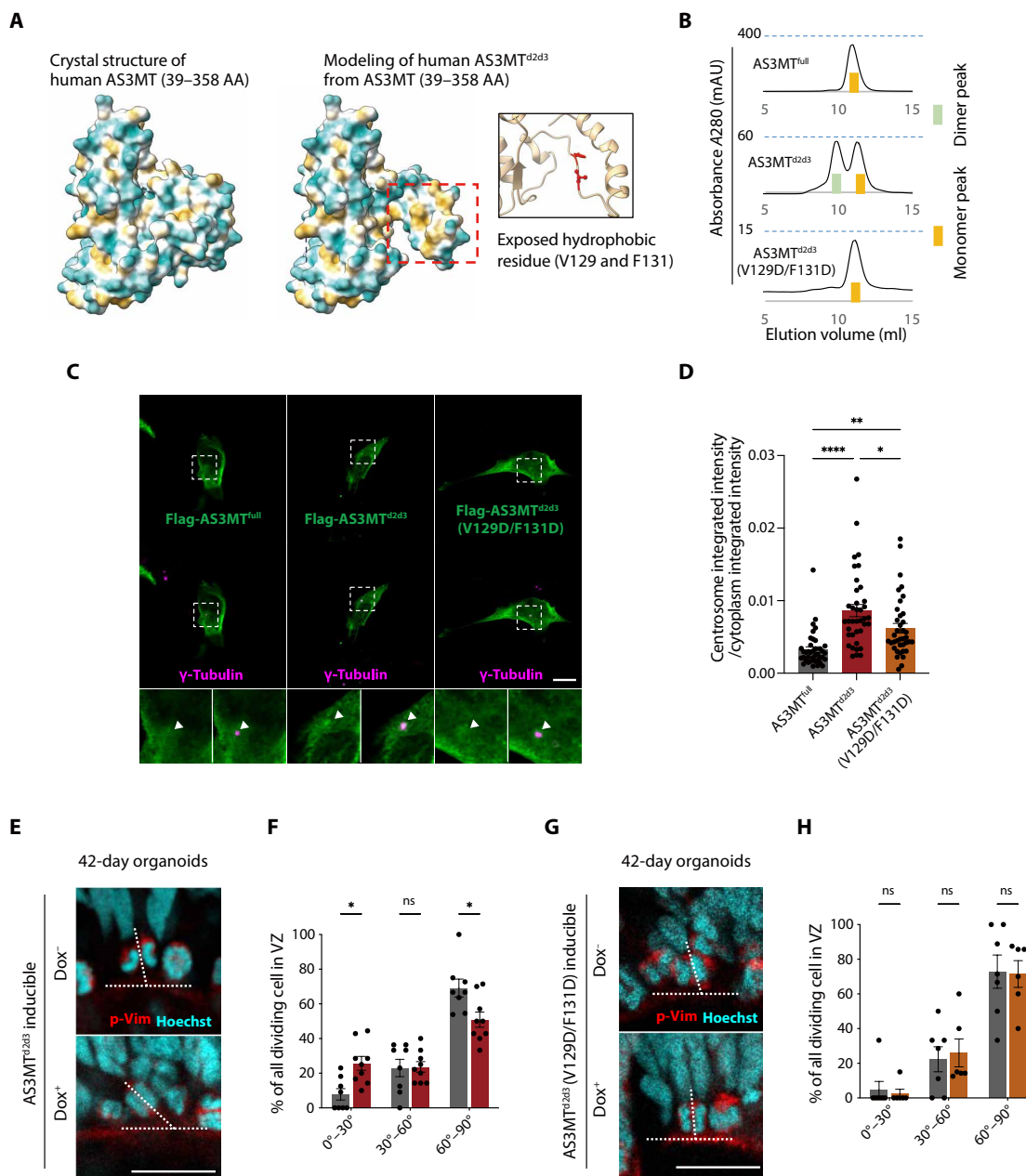
Fig. 5. Exposed hydrophobic residues of AS3MT^d2d3 drive centrosome localization and spindle misorientation. (**A**) Human AS3MT protein structure (39 to 358 AA) and deletion model (AS3MT^d2d3) with surface analysis (hydrophobic residues, yellow; hydrophilic residues, blue). (**B**) 75S size exclusion chromatography [top, AS3MT^full; middle, AS3MT^d2d3; bottom, AS3MT^d2d3 (V129D/F131D)]. (**C**) Representative image of the subcellular localization of Flag-AS3MT^full, Flag-AS3MT^d2d3, or Flag-AS3MT^d2d3 (V129D/F131D) in HEK293FT cell line, stained as indicated. The arrowheads indicate centrosome site in magnified images. (**D**) Quantification of the centrosome-integrated intensity divided by cytoplasm-integrated intensity [AS3MT^full, $n = 39$; AS3MT^d2d3, $n = 38$; AS3MT^d2d3 (V129D/F131D), $n = 38$]. (**E**) Representative images of the mitotic cell with a dividing plane from 42-day AS3MT^d2d3 inducible organoids. (**F**) Percentage of cortical progenitors within each 30° interval (not treated #1 line, $n = 8$; doxycycline-treated #1 line, $n = 9$). (**G**) Representative images of the mitotic cell with a dividing plane from 42-day AS3MT^d2d3 (V129D/F131D) inducible organoids. (**H**) Percentage of cortical progenitors within each 30° interval (not treated #10 line, $n = 7$; doxycycline-treated #10 line, $n = 6$). Scale bars, (C) 10 μm and [(E) and (G)] 20 μm. Bar graphs show the means ± SEM. Statistical significance is defined by one-way ANOVA for centrosome localization analysis and two-way ANOVA for spindle orientation analysis with Bonferroni's post hoc test for comparisons among multiple groups; *$P < 0.05$; **$P < 0.01$; ****$P < 0.0001$. Dox, doxycycline.

of ACC has been reported in patients with SZ (*45*, *46*). Structural or functional alterations in ACC are closely linked to prominent changes in social behavior (*47*), supporting the notion that the social deficits observed in AS3MT^{d2d3}-Tg mice may be associated with the changes in the neuronal population within ACC. In addition, ACC has a circuit connected to the mediodorsal thalamus (MDT), facilitating communication between prefrontal cortex and MDT. ACC neurons projecting to MDT play a crucial role in PPI (*48*). Therefore, the observed PPI deficits in our study may be linked to the changes in ACC layer composition, as indicated by snRNA-seq analysis. In light of these findings, we postulate the hypothesis that aberrant reduction of excitatory neuronal populations resulting from ectopic AS3MT^{d2d3} expression during early cortical development may contribute to abnormal sociability and sensorimotor gating observed in patients with SZ. This hypothesis warrants further investigation for detailed understanding.

Our observation of mitotic spindle misorientation associated with elevated AS3MT^{d2d3} expression and its connection to a reduction in the Tshz2^{+} cell population is intriguing. Although previous studies do not always equate mitotic spindle misorientation with stem cell depletion (*49*), our experimental conditions demonstrated a decrease in stem cell fate, aligning with recent findings on spindle orientation (*23*, *50*). This suggests that mitotic spindle misorientation, along with stem cell depletion, represents a mechanistically linked phenotype in our AS3MT^{d2d3}-Tg mouse model, contributing to a reduced proportion of specific neuronal populations following development (*51*). However, the mechanisms underlying the selective reduction of certain cell populations, such as Tshz2^{+} cells in the adult brain, remain unclear and may reflect subtle deficits similar to those observed in patients with SZ (*52*, *53*). This partial depletion could result from region-specific or temporally restricted developmental defects (*23*). Future research should aim to define the precise developmental windows and brain regions affected by AS3MT^{d2d3} expression to better understand the phenotypic consequences observed in this model.

The prevalence of alternative splicing isoforms in the mammalian brain underscores their pivotal role in shaping neuronal function as these isoforms often exhibit unique protein structures that regulate their dynamics (*54*–*56*). These isoforms provide distinct protein-protein interaction interfaces that can be critical in various cellular contexts. For instance, *Ninein* gene harbors alternative exon 18 and exon 29 that encode protein region crucial for its centrosomal localization. These exons provide binding sites for CEP170 or CEP250, creating a unique interaction interface that influence cell fate decisions during neurogenesis and cortical development. Another example is S100B (S100 calcium–binding protein B), one of the most abundant metal-binding proteins in the brain. A specific isoform of *S100B* lacks 11 of the 31 interface residues, impairing its dimerization ability but conferring an alternative function by actively inhibiting amyloid-β aggregation (*57*). These cases illustrate the far-reaching impact of alternative splicing on neuronal function. Here, we investigated the alternative splicing isoform of the *AS3MT* gene, AS3MT^{d2d3}, which exhibits distinct molecular characteristics compared to its full-length counterpart. The structural and functional differences of AS3MT^{d2d3}, such as exposed hydrophobic residues critical for dimerization and centrosome localization, may impart specific roles in spindle orientation and cortical development. Our interactome analysis from co-IP/MS supports the unique molecular interaction of AS3MT^{d2d3}, with NPM1 emerging as a candidate functional partner in modulating spindle dynamics. Together, further exploration of the mechanisms underlying these molecular characteristics is warranted to gain a deeper understanding of the role of AS3MT^{d2d3} in SZ pathology and its impact on cortical development.

AS3MT^{d2d3}'s localization to the centrosome also spurs speculation of its potential role in ciliary function. Centrosomes serve as basal bodies for primary cilia, key integrators of extracellular signaling pathways, including Wnt and Sonic hedgehog (Shh) pathways. Recent research underscores the role of primary cilia in regulating cortical development via Wnt and Shh signaling, which is pivotal for neuronal differentiation and migration (*58*). Given that ciliary dysfunction has been implicated in neurodevelopmental disorders such as SZ, defects in primary cilia may link centrosomal abnormalities to disrupted signaling cascades in this condition (*59*). Therefore, future investigations into the molecular mechanisms of AS3MT^{d2d3}'s impact on ciliary structure and signaling may help further clarify its potential relevance to SZ.

Recent genetic and epigenetic studies emphasize the pivotal role of prenatal development in the predisposition of SZ (*60*–*62*). Specifically, studies using iPSC and organoids derived from patients with SZ have consistently indicated disturbances in cell fate determination during this crucial developmental stage (*44*, *63*–*65*). Our findings contribute to this body of research, revealing that AS3MT^{d2d3} affects spindle orientation and cell fate determination, ultimately altering the neuronal composition in the adult mouse brain. This suggests a potential link between the centrosome/spindle organization affecting cell fate determination and neurodevelopmental aspects of SZ. For example, chromosome 16p13.11 duplication, a well-known genetic risk variant associated with SZ (odds ratio = 1.84), has been shown to disrupt spindle orientation and cell fate determination in patient-derived organoids (*66*, *67*). Further, PCM1, a centrosomal protein identified as closely associated with SZ (*68*), plays a crucial role in neurogenesis. The loss of PCM1 results in premature neurogenesis and depletion of the NSC pool, leading to inadequate neuron production and abnormal ventricle expansion (*69*, *70*). Our results underscore the importance of maintaining a balanced neuronal composition and offer an insightful perspective on the pathobiology of SZ by linking disrupted cell fate regulation during early development to the disorder's neurodevelopmental origins.

MATERIALS AND METHODS
Animals
All animal procedures were ethically approved by the Institutional Animal Care and Use Committee of Pohang University of Science and Technology (POSTECH-2019-0025, POSTECH-2020-0008, POSTECH-2020-0022, POSTECH-2021-0110, POSTECH-2022-0087, POSTECH-2022-0086, POSTECH-2023-0096, and POSTECH-2024-0092). All experiments were carried out in accordance with the approved guidelines. C57BL/6 mice were purchased from Hyochang Science (Daegu, South Korea) and used for in utero electroporation surgery. The AS3MT^{d2d3}-conditional expressing mice (*Rosa26* LoxP-STOP-loxP-mAS3MT^{d2d3}-IRES-mCherry) were generated through Cyagen (Beijing, China). The *Emx1*-cre mice (the Jackson Laboratories, stock #005628) were crossed with AS3MT^{d2d3}-conditional expressing mice. All mice were maintained in a specific pathogen–free facility under a 12:12-hour day/night illumination cycle. The animals were euthanized by cervical dislocation after inhalation anesthesia. Only male mice were analyzed in all the experiments.

Behavioral analyses

PPI test

PPI was measured using the SR-LAB Startle Response System following established protocols (71). The mice underwent a 5-min acclimation period in the PPI apparatus with a constant 65-dB white-noise background. Following this, the testing session began automatically. Each session involved 10 blocks with six types of trials: null (no stimulus), startle only (120 dB), and startle with a prepulse at various intensities above the baseline (69, 73, 77, or 81 dB). The trials were presented in a pseudorandomized order, ensuring that each trial type appeared once per block. The %PPI was calculated using the formula: $100 - [($response on prepulse-pulse trials / startle response on pulse-only trials$) \times 100]$.

Three-chambers social interaction test

The social interaction test involved two 10-min phases and took place in a transparent Plexiglas rectangular arena (60 cm L by 45 cm W by 40 cm H) divided into three chambers (each 45 cm L by 20 cm W by 40 cm H). During habituation, the test mice were placed in the central chamber and could freely explore all chambers. In the social phase, an unfamiliar mouse was introduced under an inverted wire cup in one of the two side chambers, and the test mice were again allowed to explore. Behavior was recorded by an overhead charge-coupled device (CCD) camera and analyzed using SMART v3.0 (Panlab) tracking software (72).

Y maze

A Y maze, consisting of three equally spaced arms (30 cm L by 15 cm H by 7 cm W, labeled A, B, and C), served as the apparatus. The mice were placed at the maze's center and allowed free movement for 8 min. The sequence of arm entries was recorded, with an alternation defined as entry into all three arms consecutively. The maximum possible alternations equaled the total number of arm entries minus two. The percentage of alternations was calculated as (actual alternations / maximum alternations) × 100, alongside recording the total arm entries.

Nesting behavior

Nest-building behavior, associated with self-care in SZ models (73), was assessed by providing single-housed mice with a new nestlet (Ancare, catalog no. 10279-140) daily. The following morning, the quality of the nest was rated on a five-point scale (74), with scores as follows: 1 = nestlet not noticeably touched, 2 = nestlet partially torn up, 3 = mostly shredded but no identifiable nest site, 4 = an identifiable but flat nest, 5 = a well-defined nest with walls >mouse body height. The average score over 6 days was analyzed using the Mann-Whitney test.

Open-field test

Spontaneous activity was assessed in an open-field arena, a white rectangular box (60 cm L by 40 cm W) with 20-cm-high walls. The mice were allowed to explore freely for 15 min starting from the center of the arena. Movements were recorded via an overhead CCD camera and analyzed by SMART v3.0 (Panlab).

Elevated plus maze

The maze featured two open arms and two closed arms (each 10 cm W by 50 cm L) elevated 60 cm above the floor. The mice were placed at the maze center, facing a closed arm, and allowed to explore for 10 min. Behavior in each arm was recorded and analyzed using SMART v3.0 (Panlab). The maze was cleaned with 70% ethanol between tests to prevent any olfactory cues from influencing behavior.

Immunocytochemistry and IHC

For immunocytochemistry, transfected cells were washed with phosphate-buffered saline (PBS) and fixed with 4% paraformaldehyde in PBS for 10 min. The additional fixation with iced ethanol 50, 75, and 95% for 5 min on ice, respectively, were followed if needed. The cells were permeabilized with 0.2% Triton X-100 in PBS for 10 min and incubated in the blocking solution (5% goat serum in PBS) for 1 hour at room temperature (RT). The cells were incubated with primary antibodies at 4°C overnight and washed three times with PBS for 10 min. Incubation with secondary antibodies for 1 ~ 2 hours at RT was followed depending on each experimental purpose. For nuclear staining, the samples were incubated with Hoechst solution for 5 min. Last, coverslips were placed on slide glasses and fixed with mounting media (Biomeda).

For IHC, harvested brains were perfused with PBS and fixed with 4% paraformaldehyde in PBS overnight, followed by cryoprotected with 30% sucrose in PBS for more than 2 days. Brains were frozen with OCT solution (Leica Biosystems) and sectioned using cryostats (Leica Biosystems) with 10- ~ 100-μm thickness depending on the experimental purpose (20 μm for slide-mounted immunostaining, 30 μm for floating immunostaining, and 100 μm for ipsilateral branching analysis). Then, dissected tissue was fixed to Superfrost Plus microscope slides (catalog no. 22037246, Thermo Fisher Scientific) and dried at RT. The dissected tissues were examined with fluorescent microscopy to confirm the electroporated cells with fluorescence. Dried samples were washed three times with PBS and permeabilized with 0.2% Triton X-100 in PBS for 10 min. If the antigen retrieval process is needed, the sections were at 95°C for 10 min with a citrate buffer of pH 6.0. Blocking was conducted with CAS-Block histochemical reagent (catalog no. 008120, Thermo Fisher Scientific) for 1 hour at RT. Samples were incubated with primary antibody mixtures at 4°C overnight and incubated with secondary antibody mixtures for 1 ~ 2 hours at RT. For nuclear staining, samples were incubated with Hoechst (0.002 mg/ml) in PBS solution for 20 min. Last, slides were fixed with mounting media (Biomeda) or Aqua-Poly/Mount (catalog no. 18606-20, Polysciences). Images of brain tissue samples were acquired using confocal microscopy with z-stacks of 0.5- ~ 1-μm intervals after confirming the electroporated regions by fluorescence signals. Each z-stack image and a merged z-projection image were compared to discriminate the cell periphery.

Chromogenic ISH targeting single exon junction (BaseScope)

Single-molecule chromogenic ISH targeting a single exon junction was performed with BaseScope Duplex Detection Reagent Kit (catalog no. 323800 ACD) as described previously (14). Forty-two–day organoids were sectioned using cryostats (Leica Biosystems) with 10-μm thickness. The sections were incubated with various combinations of two BaseScope probes such as *SOX2*, *TUBB3*, *AS3MT*-E2E3, and *AS3MT*-E1E4 (catalog nos. 719611, 1321881-C1, 716351, and 716341, ACD). The sections were imaged using a LEICA DM750 C light microscope with 40× objective lens. In the VZ of rosettes, the number of AS3MT full+/d2d3+ cells (red dots) were calculated in relation to SOX2+ cells (green dots). Similarly, in the cortical region of rosettes, AS3MT full+/d2d3+ cells were quantified with respect to TUBB3+ cells (green dots). The parameter used was the ratio of red dots to the number of cells with green dots. A total of 5 to 10 hFOs were analyzed per group.

Histological sample preparation and image analysis

Brain tissues were collected and fixed in 4% paraformaldehyde solution at 4°C overnight. Tissues were embedded in paraffin blocks, sectioned at 3-μm thickness, deparaffinized, and dehydrated via sequential addition of xylene, 100% ethanol, and 95% ethanol. The sections were then washed in distilled water and stained with hematoxylin (catalog no. HHS32, Sigma-Aldrich) and eosin (catalog no. HT110132, Sigma-Aldrich). Sections were imaged using a LEICA DM750 C light microscope. All brain areas were analyzed by Adobe Photoshop and ImageJ in section-matched tissue.

Images were obtained by using FV3000 confocal laser scanning microscope (Olympus) with 10× [0.4 numerical aperture (NA)], 20× (0.75 NA), 40× (0.95 NA), 60× (1.35 NA), or 100× (1.4 NA) objective lens. Because of the limitation of the confocal microscopy resolutions (≥230 nm for 100× and ≥240 nm for 60×), brightness and contrast were adjusted for the clarity of the images. Color scales were also carefully adjusted to avoid the potential overlap of the red and green signals. Acquired images were analyzed with Image J (Fiji) software (RRID: SCR_002285, National Institute of Health, Bethesda, MD, USA), CellSens software (Olympus), or QuPath (v0.5.1).

For migration and morphology analysis, RFP intensity was adjusted to show the clear morphology of each neuron, avoiding excessive saturation in soma regions to minimize difficulties in discriminating individual cells. Cell counting was performed in each subventricular zone/ VZ, intermediate zone (IZ), and cortical plate (CP) area and each cell shape as described previously (75).

For the analysis of axon formation and ipsilateral branching, GFP vector and target DNA are mixed 1:1 ratio to visualize the axon. GFP signals were used for axon quantification after confirming the colocalization. For axon length analysis, reference length was defined from the electroporated region to the midline of corpus callosum (CC) for normalization. The analyzing length was defined from the midline of CC to the end of the connected axon signal. For ipsilateral branching, the region of interest (ROI) was defined in the electroporated region without nonmigrating cells in the ROI and analyzed with the Fiji Plot Profile. The intensity of the fluorescence was normalized by subtracting the fluorescence intensity measured in the darkest brain region (76).

Magnetic resonance imaging

The animal MRI study was performed using a 9.4T Bruker ClinScan system (Bruker BioSpin MRI GmbH, Germany) with an actively shielded 12-cm diameter gradient insert operating with a maximum strength of 66 Gauss/cm and a rise time of 141 μs as described (77). A quadrature birdcage coil (72-mm inner diameter) was used for excitation, and an actively decoupled Bruker planar surface coil (15-mm inner diameter) positioned on top of the mouse's head was used for detection. The magnetic field homogeneity was globally shimmed with the field map method, and then a local shim was optimized using the MAPSHIM protocol with an ellipsoid shim volume covering the cerebrum (ParaVision 6, Bruker BioSpin). The animals were anesthetized and maintained with 1.5 to 2% isoflurane during the experiments. Transverse T2-weighted turbo rapid acquisition with refocused echoes spin echo images was acquired for volume measurements (repetition time/echo time = 5065/9 ms, field of view = 20 × 20 mm, matrix = 256 256 pixels, number of averages = 5, thickness = 0.25 mm, and scan time = 13.30 min). Five- to six-month-old mice were used for this analysis.

hESC culture and gene editing

Human embryonic stem cell (hESCs) were cultured in StemFlex medium (catalog no.A3349401, Gibco) by following the manufacturer's instructions. For gene editing, cloning to the donor vector, pAAVS1-Puro Xlone-eGFP (catalog no. 136936, Addgene), was performed using restriction enzymes from NEB and T4 DNA ligase from NEB, and Gibson cloning was performed using Gibson Assembly Master Mix (NEB). hESCs were harvested using Accutase solution (catalog no.A1110501, Gibco) and 1.2×10^6 cells resuspended in Opti-MEM medium were electroporated with 8 μg of donor plasmids and 2 μg of each zinc-finger nuclease–encoding plasmid (NEPA21 electroporator and 2-mm gap cuvettes, catalog no. EC-002S, Nepa gene). The cells were subsequently plated on Matrigel matrix (catalog no. 354230, Corning) in StemFlex medium supplemented with Revitacell (catalog no. A2644501, Thermo Fisher Scientific) for the first 24 hours. Individual colonies were picked and expanded after puromycin (P8833-25 mg, Sigma-Aldrich) selection (0.5 μg/ml) 7 days after electroporation.

Antibodies

Anti-FLAG rabbit polyclonal and mouse monoclonal (catalog no. F7425 and catalog no. F1804, Sigma-Aldrich), anti-FLAG rat monoclonal (catalog no. MA1-142, Thermo Fisher Scientific), anti–α-tubulin mouse monoclonal (catalog no. 66031-1-Ig, Proteintech Group), anti-BrdU rabbit polyclonal (catalog no. PA5-32256, Invitrogen), anti-BrdU mouse monoclonal (catalog no. sc-32323, Santa Cruz Biotechnology), anti–hemagglutinin (HA) rabbit polyclonal (catalog no. A190-108A, RRID:AB_67465, Bethyl Laboratories), anti-cre mouse monoclonal (catalog no. ab24607, Abcam), anti-SOX2 (catalog no. ab5603, Merck Millipore), anti–γ-tubulin mouse monoclonal (catalog no. sc-17787, Santa Cruz Biotechnology and catalog no. T5326, Sigma-Aldrich) and rabbit polyclonal (catalog no. ab11317, Abcam), anti-Tshz2 rabbit polyclonal (catalog no. 140189, Abcam), anti-NeuN mouse monoclonal (catalog no. MAB377), anti-NeuN guinea pig (catalog no. ABN90P, Merck Millipore), anti-Tuj1 mouse monoclonal (catalog no. MMS-435P), anti-Cux1 rabbit polyclonal (catalog no. 11733-1-AP, ProteinTech), anti-Ctip2 rat monoclonal (catalog no. ab18465, Abcam), anti-Satb2 mouse monoclonal (catalog no. ab51502, Abcam), anti-GABA rabbit polyclonal (catalog no. A2052, Sigma-Aldrich), anti–caspase-3 rabbit polyclonal (catalog no. 9662, Cell Signaling Technology), anti–Tbr2 rabbit polyclonal (catalog no. AB2283, Merck Millipore), anti-Pax6 mouse monoclonal (catalog no. AB_528427, DSHB), anti-Tbr1 rabbit polyclonal (catalog no. ab31940, Abcam), anti–cleaved caspase-3 rabbit polyclonal (catalog no. 9661, Cell Signaling Technology), anti-ASPM rabbit polyclonal (catalog no. IHC-00058, Thermo Fisher Scientific), anti-CDK5RAP2 rabbit polyclonal (catalog no. IHC-00063, Bethyl Laboratories), anti-WDR62 rabbit polyclonal (catalog no. A301-560A, Thermo Fisher Scientific), and anti–p-VIM (S55) (catalog no. DO76-3, MBL) were used for immunofluorescence and immunoblotting. Horseradish peroxidase (HRP)–conjugated sheep anti-mouse immunoglobulin G (lgG, catalog no. NA931, GE Healthcare) and donkey anti-rabbit IgG (catalog no. NA934, GE Healthcare) were used as secondary antibodies for immunoblotting. Alexa Fluor 405–, Alexa Fluor 488–, Alexa Fluor 568–, and Alexa Fluor 647–conjugated goat anti-mouse IgG (catalog no. A-31553, catalog no. A-11001, catalog no. A-11004, and catalog no. A-21236, Molecular Probes), anti-rabbit IgG (catalog no. A-31556, catalog no. A-11008, catalog no. A-11036, and catalog no. A-21244, Molecular

Probes), anti-rat IgG (catalog no. A-11006 and catalog no. A-11077, Molecular Probes), and anti–guinea pig IgG (catalog no. A-21450, Molecular Probes) were used as secondary antibodies for immunocytochemistry and IHC.

Plasmids

pFLAG-CMV2 (Sigma-Aldrich) and pcDNA3.1/HA (Invitrogen) were used for human AS3MT^{full}/AS3MT^{d2d3}/AS3MT^{d2d3}(V129D/F131D) and mouse AS3MT^{full}/AS3MT^{d2d3} cloning. FLAG-tagged AS3MT^{d2d3} cloned in pCIG2-mRFP was used for in utero electroporation, and HA-tagged AS3MT^{d2d3} cloned in pCIG2-EGFP was used for organoid electroporation. Human and mouse AS3MT^{full}/AS3MT^{d2d3} cDNA were amplified by polymerase chain reaction (PCR). Human and mouse AS3MT cDNA clones (NCBI reference sequence: NM_020682.4 and NM_020577.3, respectively) were amplified by PCR, cloned into the vectors, and verified by sequencing. Oligonucleotide sequence for the mouse Vim shRNA was 5′- ATGTTTTGGATCTCATCCT-GC-3′. Oligonucleotide sequence for the mouse Npm1 shRNA was 5′- ATCTTCATCTTCAGACTCTGC-3′. These oligonucleotides were annealed and ligated into the pLentiLox3.7 vector using PstI and XhoI sites. The primer information is in table S3.

Cell line culture

HEK293FT cells were cultured with Dulbecco's Modified Eagle's Medium (DMEM, Welgene) supplemented with 10% (v/v) FBS (fetal bovine serum, Merck Millipore) and 1% (v/v) Antibiotic-Antimycotic (Gibco). Cell lines were authenticated by the short tandem repeat profiling method. Cell lines were tested as negative for mycoplasma contamination.

Transfection

HEK293FT cells were transfected with polyethyleneimine (PEI) solution (1 mg/ml stock) or Lipofectamine 2000 (Invitrogen) by following the manufacturer's instructions. Cell confluencies (60 ~ 80%) were adjusted according to the experimental purposes. After 12 hours of cell plating, cell conditions and confluencies were monitored by light microscopy. Amounts of total DNA (microgram per well) were varied by culture sizes (700 to 1400 ng in 12-well plates and 7 to 14 µg in 10-cm culture dish). One microgram of DNA and 3 µl of PEI or 1 µl Lipofectamine 2000 were mixed with Opti-MEM (Gibco). The mixtures were incubated for 15 min at RT. The medium was replaced with a culture medium 3 to 5 hours after transfection.

IP/MS analysis

All procedures are performed as described previously (78) with minor modifications. For immunoprecipitation, cells were harvested 24 hours after transfection in cold PBS and centrifuged at 800g. The cells were lysed with a lysis buffer containing 50 mM tris-HCl (pH 7.4), 150 mM NaCl, 5 mM EDTA, 0.2% Triton X-100, and the inhibitor cocktail of proteases (catalog no. PIA32963, Thermo Fisher Scientific) and supplement chemicals [2 mM Nappi, 20 mM NaF, 10 mM Na$_3$VO$_4$, and 2 mM dithiothreitol (DTT)]. FLAG vector or FLAG-AS3MT^{full} or FLAG-AS3MT^{d2d3} and their respective interacting proteins were pulled down with anti-FLAG antibody immobilized on agarose beads (catalog no. A2220, Sigma-Aldrich). For in-solution digestion, eluted proteins were lyophilized and solubilized in a digestion solution containing 6 M urea and 40 mM ammonium bicarbonate in high-performance liquid chromatography–grade water (catalog no. 7732-18-5, J.T Baker). The proteins were reduced

with 5 mM tris (2-carboxyethyl) phosphine hydrochloride for 1 hour and then alkylated with 25 mM iodoacetamide in the dark for 30 min at RT. The sample was in-solution digested with sequencing-grade modified trypsin (5 ng/ml; catalog no. V5111, Promega) for 16 hours at 37°C. For mass spectrometry, tryptic peptides after in-solution digestion were separated using a homemade microcapillary column (75 µm by 12 cm) packed with C18 resin (Michrom Bioresources, USA). Samples were eluted using a linear gradient mixture of solvents A (0.1% formic acid in 2% acetonitrile) and B (0.1% formic acid in 98% acetonitrile) where the percentage of the latter mobile phase increased over 120 min at a flow rate of 0.26 µl/min: 2 to 50% for 94 min, 50 to 90% for 6 min, 90% for 6 min, 90 to 2% for 6 min, and 2% for 8 min. Eluted peptides were analyzed by use of an LTQ Velos Orbitrap mass spectrometer (Thermo Finnigan, USA) with a nano-electrospray ionization.

Double thymidine block and astral microtubule analysis

To analyze astral microtubules, HEK293 cells were first arrested by double thymidine block at the G$_1$-S boundary. Thymidine (2.5 mM; catalog no. T1895, Sigma-Aldrich) was treated for 16 hours and washed twice with PBS. After washing thymidine, the cells were incubated with DMEM/10% FBS with 1% A/A for 4 hours and transfected with FLAG-CMV2 vector or FLAG-AS3MT^{d2d3} for 5 hours. We repeated thymidine block and washing once again. After 4 hours, the HEK293 cells were treated with MG132 (10 µg/ml; catalog no. 474790, Sigma-Aldrich) for 4 hours. After that, the cells were fixed and immunostained with specific antibodies. For analysis, astral microtubules were analyzed in metaphase cells. The number and length of astral microtubules per spindle pole were measured manually and analyzed in the Cell Sens software.

Immunoblotting

Mouse cortex tissues or transfected cells were washed with 1× PBS and lysed with 1× erythrocyte lysis buffer [50 mM tris (pH 8.0), 250 mM NaCl, 0.1% NP-40, 5 mM EDTA, 2 mM sodium pyrophosphate, 5 mM NaF, 2 mM Na$_3$VO$_4$, 1 mM DTT, and protease inhibitor cocktail (Roche)]. Ultrasonication was used for complete lysis. For immunoblotting, 5× SDS sampling buffer [2% SDS, 60 mM tris (pH 6.8), 24% glycerol, 0.1% bromophenol blue, and 5% β-mercaptoethanol was added, and the mixtures were boiled at 100°C for 10 min. SDS–polyacrylamide gel electrophoresis was performed with 12% polyacrylamide gel in an electrophoresis tank (Bio-Rad) and transferred to polyvinylidene difluoride membrane (Merck Millipore). Transferred membranes were blocked with 5% skim milk in tris-buffered saline [20 mM tris (pH 8.0) and 137.5 mM NaCl] with 0.25% Tween20 for 0.5 ~ 1 hour at RT. The primary antibody was mixed with skim milk following the manufacturer's guide, and membranes were incubated at 4°C overnight. The membranes were further incubated with HRP-conjugated secondary antibodies for 1.5 hours at RT, and protein signals were detected by enhanced chemiluminescence solutions (Bio-Rad) in the image analyzer (Azure Biosystems).

Sucrose-gradient centrifugation for centrosomal fractionation

Centrosome isolation was performed by sucrose gradient velocity sedimentation as described (79, 80). Briefly, confluent cells were incubated at 37°C for 3 hours with 10 µg/ml final concentration of nocodazole (Sigma-Aldrich) and successively washed with ice-cold PBS, 8% sucrose in 1/10 diluted PBS, and 8% sucrose in distilled

water (DW). The cells were then lysed with buffer A [50 mM tris (pH 7.4), 80 mM NaCl, 25 mM EDTA (pH 8.0), and 1% Triton X-100] plus protease inhibitor for 10 min on ice with vigorous rotation. After incubation overnight at 4°C, the lysate was sonicated for 10 strokes at low output with a microtip and subjected to two passages through a 23-gauge needle and one filtration through a 40-μm Nylon mesh (BD Falcon). The filtrate was cleared by centrifugation at 2500g for 10 min, and the supernatant was incubated in 10 mM Hepes and deoxyribonuclease I (2 μg/ml) for 30 min at 0°C. The supernatant was laid on top of 2 ml of 60% sucrose cushion and subject to centrifugation at 10,000g for 30 min. The 60% sucrose fraction containing centrosomes was recovered and diluted to 30% with distilled water, which was then added on top of a discontinuous sucrose gradient (from the bottom to the top, containing 1.7, 1, and 1 ml of 70, 50, and 40% sucrose solutions, respectively) in a 13-ml 41Ti Beckman ultraclear tube. After centrifugation at 40,000g for 1 hour and 15 min, 20 fractions (400 μl each) were collected, starting from the bottom of the gradient. The fractions were frozen in liquid nitrogen and then stored at −80°C for future use.

In utero electroporation
Pregnant C57BL/6 mice at 13.5 were anesthetized with an isoflurane (induction in a chamber: 2.8%, surgery via mask: 2.5%, Hana Pharm Corporation, Gyeonggi-do, South Korea). Coding sequences of target genes in pCIG2 vectors were purified by using EndoFree plasmid maxi kit (Qiagen, Germantown, MD, USA). Each DNA solution (2 ~ 3 μg/μl) mixed with Fast Green solution (0.1%) was injected into bilateral ventricles of the embryo through pulled microcapillary tube (Drummond Scientific, Broomall, PA, USA). Tweezer-type electrode containing two disc-type electrodes was located at appropriate angle, and electric pulses were given as 35 V, 50 ms, five times with 950-ms intervals by using an electroporator (Harvard Apparatus, Holliston, MA, USA). After electroporation, the embryos were put back into the mother's abdomen, the incision was sutured, and the mice were turned back to their home cage. To analyze cell proliferation or neuronal differentiation, BrdU (Sigma-Aldrich) was administered at E14.5 by intraperitoneal injection (50 mg/kg in PBS). The mice were euthanized at E14.5, E15.5, E18.5, or P6. To minimize the sample-by-sample variation, we analyzed the samples in the comparable tissue quality, transfected region, and total transfection efficiency in each experimental set.

Forebrain organoid culture and electroporation
Brain region–specific cerebral organoid culture was prepared following the previous report (81). We maintained hESC (WA09, WiCell, USA) by mouse embryonic fibroblast–dependent culture with stem cell culture media [DMEM/F12 (Gibco), 20% knockout serum replacement (KOSR, Gibco), 1× GlutaMax (Gibco), 1× nonessential amino acid solution (NEAA, Gibco), 1× penicillin-streptomycin (HyClone), 1× β-mercaptoethanol (Gibco), and basic fibroblast growth factor (10 ng/ml; Peprotech)].

To establish forebrain organoid, we detached 1- ~ 1.5-mm sized WA09 stem cell colonies by 30-min treatment of collagenase IV (Thermo Fisher Scientific, 17104019, 1 mg/ml, dissolved in DMEM/F12). The duration of collagenase IV treatment was increased up to 2 hours until colonies were detached. Detached stem cell colonies were transferred to ultralow attachment six-well plate (Corning) and cultured for 4 days with Forebrain first media [DMEM/F12, 20% KOSR, 1× GlutaMax, 1× NEAA, 1× β-mercaptoethanol, 1×

penicillin-streptomycin, 2 μM dorsomorphin (Stem Cell Technologies), and 2 μM A-83 (Stem Cell Technologies)]. On culture days 5 and 6, half of the media was replaced with Forebrain second media [DMEM/F12, 1× N2 supplement, 1× GlutaMax, 1× NEAA, 1× penicillin-streptomycin, 1 μM CHIR-99021 (Stem Cell Technologies), and 1 μM SB-431542 (Stem Cell Technologies)]. On culture day 7, embryonic bodies were embedded into a mixture of Matrigel (Corning) and Forebrain second media (3:2 ratio). The mixture was spread on an ultralow attachment plate and incubated at 37°C for 30 min to solidify. Organoids were further cultured for 7 days with Forebrain second media. On culture day 14, Matrigel was mechanically broken by two or three times of pipetting with 10-ml pipet. Organoids were further cultured with Forebrain third media [DMEM/F12, 1× N2 supplement (Gibco), 1× B27 supplement (Gibco), 1× GlutaMAX, 1× NEAA, 1× β- mercaptoethanol, 1× penicillin-streptomycin, and insulin (2.5 μg/ml; Sigma-Aldrich)] and shaking (75 rpm).

For the doxycycline-inducible expression, we replaced the media with a third media including 2 μM doxycycline (Stem Cell Technologies, catalog no. 72742) on culture day 20. Organoids were further cultured with this medium until the fixation day.

For electroporation in forebrain organoids, we used organoids cultured for 50 days. DNA constructs (2 μg/μl concentration) combined with Fast green were injected into empty spaces of organoid rosettes. The injection was performed with a micro-injector (PLI-100 Pico-Injector, Harvard Apparatus) set at 10 psi and 5 ~ 20 ms of injection time. After that, electroporation was performed with an electroporator (Harvard Apparatus, Holliston, MA, USA) set at 80 V, 50-ms duration, 1-s interval, and five pulses.

Protein preparation
The human arsenite methyltransferase (AS3MT), except for its C-terminal 17 residues that are predicted to be structurally disordered and N-terminal 38 residues for suitable crystallization. This construct has a hexahistidine maltose-binding protein (MBP) tag in the pPRO MBP vector. The recombinant proteins of AS3MT were overexpressed in BL21(DE3) cell strain overnight by the addition of 1.0 mM isopropyl β-D-1-thiogalactopyranoside at 25°C when the cell density reached $A_{600 \, nm}$ of 0.8. The cells were lysed in buffer containing 20 mM Hepes (pH 7.5), 0.5 M KCl, 40 mM imidazole, 5 mM 2-mercaptoethanol (B-ME), and 0.5 mM phenylmethylsulfonyl fluoride. The soluble fraction was subjected to a nickel column. For purification of AS3MT, the eluted fusion protein was cleaved by Prescission, followed by further purification using ionic interaction chromatography (Q column ionic, GE Healthcare). Peak fractions were collected, concentrated, and subsequently applied to Superdex S75 16/600 (GE Healthcare) preequilibrated with a buffer containing 20 mM Hepes (pH 7.5), 150 mM KCl, and 1 mM DTT. Purified AS3MT samples were stored at −80°C at a concentration of ~15 mg/ml for future use.

Crystallization and structure determination
Human AS3MT was crystallized by the hanging-drop diffusion method. Crystals appeared in a buffer containing 0.24 M sodium malonate (pH 7.0), 20% (v/v) PEG-3350. The crystallization buffer was supplemented with glycerol or ethylene glycol to a final concentration of 15 to 20% (v/v) as a cryoprotectant before flash freezing crystals in liquid nitrogen. Diffraction data were collected on beamlines BLC5 at Pohang Accelerator Laboratory, The data were indexed, integrated, and scaled using the HKL2000, a software suite for x-ray

diffraction data processing. The structure of the human AS3MT was solved by molecular replacement using PHASER-MR, a tool for molecular replacement, as implemented in PHENIX, a comprehensive software suite for macromolecular structure determination. The molecular replacement model is the structure of an As (III) *S*-adenosylmethionine methyltransferase (PDB 4FS8) as a searching model.

scRNA-seq analysis

Gene expression tables were generated using CellRagner count (v6.1.2). The downstream analysis was performed using Seurat (v4.1.2). Briefly, the cells were removed on the basis of the following criteria: <500 genes, >99 percentile genes of nFeature_RNA, >5% mitochondrial read, >2000 unique molecular identifiers (UMIs), and <99 percentiles of UMIs.

We normalized each dataset using Seurat's NormalizeData function following parameters, "normalization.method = 'LogNormalize', scale.factor = 10000". The 2000 top highly variable genes were selected using Seurat's FindVariableFeatures function. Doublets were removed with DoubletFinder (v2.0.3).

We integrated Control and AS3MT^{d2d3}-Tg datasets for clustering and dimensionality reduction using Seurat's SelectIntegrationFeatures, FindIntegrationAnchors, and IntegrateData functions. We performed scaling the data and principal components analysis (PCA) using Seurat's ScaleData and RunPCA using 30 npcs. A shared nearest-neighbor graph was constructed using FindNeighbors function using reduction = "pca" and dims = 1:30 parameters. We identified transcriptionally distinct clusters using FindClusters using resolution = 0.8.

The following marker genes were used to assign cell types: NSC (*Hes1*); NSC_mitosis (*Hes1* and *Mki67*); IPC (*Eomes*); IPC_mitosis (*Eomes* and *Mki67*); PN1 (*Neurod1*); PN2 (*Cntn2* and *Satb2*); PN3 (*Sox5*, *Bcl11b*, *Tle4* and *Mapt*); CR (*Reln*); inhibitory (*Gad2*); MG (*Ptprc*); mural (*Pdgfrb*); and erythrocyte (*Hbb-bs*, *Hba-a1*, *Hbb-bt*, and *Hba-a2*).

Trajectory inference analysis was performed using Slingshot (ver. 2.2.1) package. To compare trajectories, we used Condiments (v0.99.14) pipeline (*20*). First, we calculated imbalance score across the conditions to find whether cells were imbalanced or not. Next, we performed differential topology test using Condiments' topologyTest function to confirm that those two conditions fit a common trajectory. Last, we performed differential progression test using Condiments' progressionTest to test differential abundance of the different conditions (for statistical analysis, Kolmogorov-Smirnov test was used). We also calculated the pseudotime of each cell and drew pseudotime boxplot to confirm which cell types were differentially abundant.

snRNA-seq analysis

The snRNA-seq analysis was done similarly to scRNA-seq analysis except for the following description. Gene expression tables were generated using CellRagner count (v6.1.2) with "--include-introns" option. Nuclei were removed on the basis of the following criteria: <500 genes, >99 percentile genes of nFeature_RNA, >1% mitochondrial read.

The following marker genes were used to assign cell types: Excitatory (*Neurod6*, *Slc17a7*, and *Nrn1*); inhibitory (*Gad1* and *Gad2*); microglia (*C1qa*, *C1qb*, *C1qc*, and *Ctss*); oligodendrocyte (*Ermn*, *Opalin*, *Mog*, and *Aspa*); OPC (*Pdgfra*, *Cacng4*, and *Matn4*); NF_Oligo (*Neu4*, *Bmp4*, and *Enpp6*); astrocyte (*Gjb6*, *Aqp4*, and *Acsbg1*); endothelial (*Flt1*); Exc_L2/3 (*Cux2* and *Calb1*); Exc_L5 (*Etv1*); and Exc_L6 (*Foxp2* and *Syt6*).

Statistical analysis

For statistical analysis, GraphPad Prism 10.0 (GraphPad Software) was used. All graphs were presented as the means ± SEM. Statistical significance of the data was analyzed by two-tailed Student's *t* test, Welch's *t* test, Kolmogorov-Smirnov test, Mann-Whitney test, or moderate *t* test for comparisons between two groups and one-way or two-way analysis of variance (ANOVA) followed by Bonferroni's post hoc test for comparisons among multiple groups. Several biological replicates, experiments, and statistical tests used for the comparison were mentioned within the figure legends and in tables S4 and S5.

Supplementary Materials

The PDF file includes:
Figs. S1 to S15
Legends for tables S1 to S5

Other Supplementary Material for this manuscript includes the following:
Tables S1 to S5

REFERENCES AND NOTES

1. R. Birnbaum, D. R. Weinberger, Genetic insights into the neurodevelopmental origins of schizophrenia. *Nat. Rev. Neurosci.* **18**, 727–740 (2017).
2. M. E. Shenton, C. C. Dickey, M. Frumin, R. W. McCarley, A review of MRI findings in schizophrenia. *Schizophr. Res.* **49**, 1–52 (2001).
3. M. A. Aghevli, J. J. Blanchard, W. P. Horan, The expression and experience of emotion in schizophrenia: A study of social interactions. *Psychiatry Res.* **119**, 261–270 (2003).
4. I. Mata, R. Perez-Iglesias, R. Roiz-Santiañez, D. Tordesillas-Gutierrez, A. Gonzalez-Mandly, A. Berja, J. L. Vazquez-Barquero, B. Crespo-Facorro, Additive effect of NRG1 and DISC1 genes on lateral ventricle enlargement in first episode schizophrenia. *Neuroimage* **53**, 1016–1022 (2010).
5. S. Ripke, C. O'Dushlaine, K. Chambert, J. L. Moran, A. K. Kähler, S. Akterin, S. E. Bergen, A. L. Collins, J. J. Crowley, M. Fromer, Y. Kim, S. H. Lee, P. K. E. Magnusson, N. Sanchez, E. A. Stahl, S. Williams, N. R. Wray, K. Xia, F. Bettella, A. D. Borglum, B. K. Bulik-Sullivan, P. Cormican, N. Craddock, C. de Leeuw, N. Durmishi, M. Gill, V. Golimbet, M. L. Hamshere, P. Holmans, D. M. Hougaard, K. S. Kendler, K. Lin, D. W. Morris, O. Mors, P. B. Mortensen, B. M. Neale, F. A. O'Neill, M. J. Owen, M. P. Milovancevic, D. Posthuma, J. Powell, A. L. Richards, B. P. Riley, D. Ruderfer, D. Rujescu, E. Sigurdsson, T. Silagadze, A. B. Smit, H. Stefansson, S. Steinberg, J. Suvisaari, S. Tosato, M. Verhage, J. T. Walters, Multicenter Genetic Studies of Schizophrenia Consortium, D. F. Levinson, P. V. Gejman, K. S. Kendler, C. Laurent, B. J. Mowry, M. C. O'Donovan, M. J. Owen, A. E. Pulver, B. P. Riley, S. G. Schwab, D. B. Wildenauer, F. Dudbridge, P. Holmans, J. Shi, M. Albus, M. Alexander, D. Campion, D. Cohen, D. Dikeos, J. Duan, P. Eichhammer, S. Godard, M. Hansen, F. B. Lerer, K.-Y. Liang, W. Maier, J. Mallet, D. A. Nertney, N. Nestadt, N. Norton, F. A. O'Neill, G. N. Papadimitriou, R. Ribble, A. R. Sanders, J. M. Silverman, D. Walsh, N. M. Williams, B. Wormley, Psychosis Endophenotypes International Consortium, M. J. Arranz, S. Bakker, S. Bender, E. Bramon, D. Collier, B. Crespo-Facorro, J. Hall, J. Iyegbe, A. Jablensky, R. S. Kahn, L. Kalaydjieva, S. Lawrie, C. M. Lewis, K. Lin, D. H. Linszen, I. Mata, A. M. Intosh, R. M. Murray, R. A. Ophoff, J. Powell, D. Rujescu, J. Van Os, M. Walshe, M. Weisbrod, D. Wiersma, Wellcome Trust Case Control Consortium 2, P. Donnelly, I. Barroso, J. M. Blackwell, E. Bramon, M. A. Brown, J. P. Casas, A. P. Corvin, P. Deloukas, A. Duncanson, J. Jankowski, H. S. Markus, C. G. Mathew, C. N. A. Palmer, R. Plomin, A. Rautanen, S. J. Sawcer, R. C. Trembath, A. C. Viswanathan, N. W. Wood, C. C. A. Spencer, G. Band, C. Bellenguez, C. Freeman, G. Hellenthal, E. Giannoulatou, M. Pirinen, R. D. Pearson, A. Strange, Z. Su, D. Vukcevic, P. Donnelly, C. Langford, S. E. Hunt, S. Edkins, R. Gwilliam, H. Blackburn, S. J. Bumpstead, S. Dronov, M. Gillman, E. Gray, N. Hammond, A. Jayakumar, O. T. M. Cann, J. Liddle, S. C. Potter, R. Ravindrarajah, M. Ricketts, A. Tashakkori-Ghanbaria, M. J. Waller, P. Weston, S. Widaa, P. Whittaker, I. Barroso, P. Deloukas, C. G. Mathew, J. M. Blackwell, M. A. Brown, A. P. Corvin, M. I. McCarthy, C. C. A. Spencer, E. Bramon, A. P. Corvin, M. C. O'Donovan, K. Stefansson, E. Scolnick, S. Purcell, S. A. McCarroll, P. Sklar, C. M. Hultman, P. F. Sullivan, Genome-wide association analysis identifies 13 new risk loci for schizophrenia. *Nat. Genet.* **45**, 1150–1159 (2013).
6. S. Ripke, B. M. Neale, A. Corvin, J. T. R. Walters, K.-H. Farh, P. A. Holmans, P. Lee, B. Bulik-Sullivan, D. A. Collier, H. Huang, T. H. Pers, I. Agartz, E. Agerbo, M. Albus, M. Alexander, F. Amin, S. A. Bacanu, M. Begemann, R. A. Belliveau Jr., J. Bene, S. E. Bergen, E. Bevilacqua, T. B. Bigdeli, D. W. Black, R. Bruggeman, N. G. Buccola, R. L. Buckner, W. Byerley, W. Cahn, G. Cai, D. Campion, R. M. Cantor, V. J. Carr, N. Carrera, S. V. Catts, K. D. Chambert, R. C. K. Chan, R. Y. L. Chen, E. Y. H. Chen, W. Cheng, E. F. C. Cheung, S. A. Chong, C. R. Cloninger, D. Cohen, N. Cohen, P. Cormican, N. Craddock, J. J. Crowley,

D. Curtis, M. Davidson, K. L. Davis, F. Degenhardt, J. D. Favero, D. Demontis, D. Dikeos, T. Dinan, S. Djurovic, G. Donohoe, E. Drapeau, J. Duan, F. Dudbridge, N. Durmishi, P. Eichhammer, J. Eriksson, V. Escott-Price, L. Essioux, A. H. Fanous, M. S. Farrell, J. Frank, L. Franke, R. Freedman, N. B. Freimer, M. Friedl, J. I. Friedman, M. Fromer, G. Genovese, L. Georgieva, I. Giegling, P. Giusti-Rodríguez, S. Godard, J. I. Goldstein, V. Golimbet, S. Gopal, J. Gratten, L. de Haan, C. Hammer, M. L. Hamshere, M. Hansen, T. Hansen, V. Haroutunian, A. M. Hartmann, F. A. Henskens, S. Herms, J. N. Hirschhorn, P. Hoffmann, A. Hofman, M. V. Hollegaard, D. M. Hougaard, M. Ikeda, I. Joa, A. Julià, R. S. Kahn, L. Kalaydjieva, S. Karachanak-Yankova, J. Karjalainen, D. Kavanagh, M. C. Keller, J. L. Kennedy, A. Khrunin, Y. Kim, J. Klovins, J. A. Knowles, B. Konte, V. Kucinskas, Z. A. Kucinskiene, H. Kuzelova-Ptackova, A. K. Kähler, C. Laurent, J. L. C. Keong, S. H. Lee, S. E. Legge, J. Lerer, M. Li, T. Li, K.-Y. Liang, J. Lieberman, S. Limborska, C. M. Loughland, J. Lubinski, J. Lönnqvist, M. M. Jr, P. K. E. Magnusson, B. S. Maher, W. Maier, J. Mallet, S. Marsal, S. Mattheisen, M. Mattingsdal, R. W. McCarley, C. M. Donald, A. M. M. Intosh, S. Meier, C. J. Meijer, B. Melegh, I. Melle, R. I. Mesholam-Gately, A. Metspalu, P. T. Michie, L. Milani, V. Milanova, Y. Mokrab, D. W. Morris, O. Mors, K. C. Murphy, R. M. Murray, I. Myin-Germeys, B. Müller-Myhsok, M. Nelis, I. Nenadic, D. A. Nertney, G. Nestadt, K. K. Nicodemus, L. Nikitina-Zake, L. Nisenbaum, A. Nordin, E. O'Callaghan, C. O'Dushlaine, F. A. O'Neill, S.-Y. Oh, A. Olincy, L. Olsen, J. Van Os, C. Pantelis, G. N. Papadimitriou, S. Papiol, E. Parkhomenko, M. T. Pato, T. Paunio, M. Pejovic-Milovancevic, D. O. Perkins, O. Pietiläinen, J. Pimm, A. J. Pocklington, J. Powell, A. Price, A. E. Pulver, S. M. Purcell, D. Quested, H. B. Rasmussen, A. Reichenberg, M. A. Reimers, A. L. Richards, J. L. Roffman, P. Roussos, D. M. Ruderfer, V. Salomaa, A. R. Sanders, U. Schall, C. R. Schubert, T. G. Schulze, S. G. Schwab, E. M. Scolnick, R. J. Scott, L. J. Seidman, J. Shi, E. Sigurdsson, T. Silagadze, J. M. Silverman, K. Sim, P. Slominsky, J. W. Smoller, H.-C. So, C. C. A. Spencer, E. A. Stahl, H. Stefansson, S. Steinberg, E. Stogmann, R. E. Straub, E. Strengman, J. Strohmaier, T. S. Stroup, M. Subramaniam, J. Suvisaari, D. M. Svrakic, J. P. Szatkiewicz, E. Söderman, S. Thirumalai, D. Toncheva, S. Tosato, J. Veijola, J. Waddington, D. Walsh, D. Wang, Q. Wang, B. T. Webb, M. Weiser, D. B. Wildenauer, N. M. Williams, S. Williams, S. H. Witt, A. R. Wolen, E. H. M. Wong, B. K. Wormley, H. S. Xi, C. C. Zai, X. Zheng, F. Zimprich, N. R. Wray, K. Stefansson, P. M. Visscher, R. Adolfsson, O. A. Andreassen, D. H. R. Blackwood, E. Bramon, J. D. Buxbaum, A. D. Børglum, S. Cichon, A. Darvasi, E. Domenici, H. Ehrenreich, T. Esko, P. V. Gejman, M. Gill, H. Gurling, C. M. Hultman, N. Iwata, A. V. Jablensky, E. G. Jönsson, K. S. Kendler, G. Kirov, J. Knight, T. Lencz, D. F. Levinson, Q. S. Li, J. Liu, A. K. Malhotra, S. A. McCarroll, A. M. Quillin, J. L. Moran, P. B. Mortensen, B. J. Mowry, M. M. Nöthen, R. A. Ophoff, M. J. Owen, A. Palotie, C. N. Pato, T. L. Petryshen, D. Posthuma, M. Rietschel, B. P. Riley, D. Rujescu, P. C. Sham, P. Sklar, D. S. Clair, D. R. Weinberger, J. R. Wendland, T. Werge, M. J. Daly, P. F. Sullivan, Biological insights from 108 schizophrenia-associated genetic loci. *Nature* **511**, 421–427 (2014).

7. M. Li, A. E. Jaffe, R. E. Straub, R. Tao, J. H. Shin, Y. Wang, Q. Chen, C. Li, Y. Jia, K. Ohi, B. J. Maher, N. J. Brandon, A. Cross, J. G. Chenoweth, D. J. Hoeppner, H. Wei, T. M. Hyde, R. McKay, J. E. Kleinman, D. R. Weinberger, A human-specific AS3MT isoform and BORCS7 are molecular risk factors in the 10q24.32 schizophrenia-associated locus. *Nat. Med.* **22**, 649–656 (2016).

8. A. Noatynska, M. Gotta, P. Meraldi, Mitotic spindle (DIS)orientation and DISease: Cause or consequence? *J. Cell Biol.* **199**, 1025–1035 (2012).

9. F. di Pietro, A. Echard, X. Morin, Regulation of mitotic spindle orientation: An integrated view, *EMBO Rep.* **17**, 1106–1130 (2016).

10. G. Fishell, A. R. Kriegstein, Neurons from radial glia: The consequences of asymmetric inheritance. *Curr. Opin. Neurobiol.* **13**, 34–41 (2003).

11. L. M. Farkas, W. B. Huttner, The cell biology of neural stem and progenitor cells and its significance for their proliferation versus differentiation during mammalian brain development. *Curr. Opin. Cell Biol.* **20**, 707–715 (2008).

12. J. T. Paridaen, W. B. Huttner, Neurogenesis during development of the vertebrate central nervous system. *EMBO Rep.* **15**, 351–364 (2014).

13. O. Durak, F. Gao, Y. J. Kaeser-Woo, R. Rueda, A. J. Martorell, A. Nott, C. Y. Liu, L. A. Watson, L.-H. Tsai, Chd8 mediates cortical neurogenesis via transcriptional regulation of cell cycle and Wnt signaling. *Nat. Neurosci.* **19**, 1477–1488 (2016).

14. Y. Takahashi, K. R. Maynard, M. Tippani, A. E. Jaffe, K. Martinowich, J. E. Kleinman, D. R. Weinberger, T. M. Hyde, Single molecule in situ hybridization reveals distinct localizations of schizophrenia risk-related transcripts SNX19 and AS3MT in human brain. *Mol. Psychiatry* **26**, 3536–3547 (2021).

15. R. W. McCarley, C. G. Wible, M. Frumin, Y. Hirayasu, J. J. Levitt, I. A. Fischer, M. E. Shenton, MRI anatomy of schizophrenia. *Biol. Psychiatry* **45**, 1099–1119 (1999).

16. C. U. Correll, N. R. Schooler, Negative symptoms in schizophrenia: A review and clinical guide for recognition, assessment, and treatment. *Neuropsychiatr. Dis. Treat.* **16**, 519–534 (2020).

17. D. L. Braff, M. A. Geyer, N. R. Swerdlow, Human studies of prepulse inhibition of startle: Normal subjects, patient groups, and pharmacological studies. *Psychopharmacology (Berl)* **156**, 234–258 (2001).

18. Z. Yao, C. T. J. van Velthoven, T. N. Nguyen, J. Goldy, A. E. Sedeno-Cortes, F. Baftizadeh, D. Bertagnolli, T. Casper, M. Chiang, K. Crichton, S.-L. Ding, O. Fong, E. Garren, A. Glandon,

N. W. Gouwens, J. Gray, L. T. Graybuck, M. J. Hawrylycz, D. Hirschstein, M. Kroll, K. Lathia, C. Lee, B. Levi, D. McMillen, S. Mok, T. Pham, Q. Ren, C. Rimorin, N. Shapovalova, J. Sulc, S. M. Sunkin, M. Tieu, A. Torkelson, H. Tung, K. Ward, N. Dee, K. A. Smith, B. Tasic, H. Zeng, A taxonomy of transcriptomic cell types across the isocortex and hippocampal formation. *Cell* **184**, 3222–3241.e26 (2021).

19. The Allen Mouse Brain Atlas, Allen Institute for Brain Science (2004); mouse.brain-map.org.

20. H. R. d. Bézieux, K. V. d. Berge, K. Street, S. Dudoit, Trajectory inference across multiple conditions with condiments: Differential topology, progression, differentiation, and expression. bioRxiv 433671 [Preprint] (2021). https://doi.org/10.1101/2021.03.09.433671.

21. J. A. Knoblich, Mechanisms of asymmetric stem cell division. *Cell* **132**, 583–597 (2008).

22. K. H. Siller, C. Q. Doe, Spindle orientation during asymmetric cell division. *Nat. Cell Biol.* **11**, 365–374 (2009).

23. S. Falk, S. Bugeon, J. Ninkovic, G. A. Pilz, M. P. Postiglione, H. Cremer, J. A. Knoblich, M. Gotz, Time-specific effects of spindle positioning on embryonic progenitor pool composition and adult neural stem cell seeding. *Neuron* **93**, 777–791.e3 (2017).

24. M. S. Lindström, NPM1/B23: A multifunctional chaperone in ribosome biogenesis and chromatin remodeling. *Biochem. Res. Int.* **2011**, 195209 (2011).

25. M. A. Amin, S. Matsunaga, S. Uchiyama, K. Fukui, Depletion of nucleophosmin leads to distortion of nucleolar and nuclear structures in HeLa cells. *Biochem. J.* **415**, 345–351 (2008).

26. S. B. Lizarraga, S. P. Margossian, M. H. Harris, D. R. Campagna, A.-P. Han, S. Blevins, R. Mudbhary, J. E. Barker, C. A. Walsh, M. D. Fleming, Cdk5rap2 regulates centrosome function and chromosome segregation in neuronal progenitors. *Development* **137**, 1907–1917 (2010).

27. D. Jayaraman, A. Kodani, D. M. Gonzalez, J. D. Mancias, G. H. Mochida, C. Vagnoni, J. Johnson, N. Krogan, J. W. Harper, J. F. Reiter, B.-I. Bae, C. A. Walsh, Microcephaly proteins Wdr62 and Aspm define a mother centriole complex regulating centriole biogenesis, apical complex, and cell fate. *Neuron* **92**, 813–828 (2016).

28. E. Di Lullo, A. R. Kriegstein, The use of brain organoids to investigate neural development and disease. *Nat. Rev. Neurosci.* **18**, 573–584 (2017).

29. L. B. Chuye, A. Dimitri, A. Desai, C. Handelmann, Y. Bae, P. Johari, J. M. Jornet, I. Klejbor, M. K. Stachowiak, E. K. Stachowiak, Brain organoids: Expanding our understanding of human development and disease. *Results Probl. Cell Differ.* **66**, 183–206 (2018).

30. T. A. Dixon, A. R. Muotri, Advancing preclinical models of psychiatric disorders with human brain organoid cultures. *Mol. Psychiatry* **28**, 83–95 (2023).

31. S. Shen, B. Lang, C. Nakamoto, F. Zhang, J. Pu, S.-L. Kuan, C. Chatzi, S. He, I. Mackie, N. J. Brandon, Schizophrenia-related neural and behavioral phenotypes in transgenic mice expressing truncated Disc1. *J. Neurosci.* **28**, 10893–10904 (2008).

32. M. Druart, M. Nosten-Bertrand, S. Poll, S. Crux, F. Nebeling, C. Delhaye, Y. Dubois, M. Mittag, M. Leboyer, R. Tamouza, M. Fuhrmann, C. L. Magueresse, Elevated expression of complement C4 in the mouse prefrontal cortex causes schizophrenia-associated phenotypes. *Mol. Psychiatry* **26**, 3489–3501 (2021).

33. D. De Pietri Tonelli, J. N. Pulvers, C. Haffner, E. P. Murchison, G. J. Hannon, W. B. Huttner, miRNAs are essential for survival and differentiation of newborn neurons but not for expansion of neural progenitors during early neurogenesis in the mouse embryonic neocortex. *Development* **135**, 3911–3921 (2008).

34. L. Magri, M. Cambiaghi, M. Cominelli, C. Alfaro-Cervello, M. Cursi, M. Pala, A. Bulfone, J. M. Garcia-Verdugo, L. Leocani, F. Minicucci, P. L. Poliani, R. Galli, Sustained activation of mTOR pathway in embryonic neural stem cells leads to development of tuberous sclerosis complex-associated lesions. *Cell Stem Cell* **9**, 447–462 (2011).

35. B. K. Puri, S. B. Hutton, N. Saeed, A. Oatridge, J. V. Hajnal, L.-J. Duncan, M. J. Chapman, T. R. Barnes, G. M. Bydder, E. M. Joyce, A serial longitudinal quantitative MRI study of cerebral changes in first-episode schizophrenia using image segmentation and subvoxel registration. *Psychiatry Res.* **106**, 141–150 (2001).

36. A. Agarwal, M. Zhang, I. Trembak-Duff, T. Unterbarnscheidt, K. Radyushkin, P. Dibaj, D. de Martins Souza, S. Boretius, M. M. Brzózka, H. Steffens, S. Berning, Z. Teng, M. N. Gummert, M. Tantra, P. C. Guest, K. I. Willig, J. Frahm, S. W. Hell, S. Bahn, M. J. Rossner, K.-A. Nave, H. Ehrenreich, W. Zhang, M. H. Schwab, Dysregulated expression of Neuregulin-1 by cortical pyramidal neurons disrupts synaptic plasticity. *Cell Rep.* **8**, 1130–1145 (2014).

37. I. Mahar, A. MacIsaac, J. J. Kim, C. Qiang, M. A. Davoli, G. Turecki, N. Mechawar, Effects of neuregulin-1 administration on neurogenesis in the adult mouse hippocampus and characterization of immature neurons along the septotemporal axis. *Sci. Rep.* **6**, 30467 (2016).

38. R. Favaro, M. Valotta, A. L. M. Ferri, E. Latorre, J. Mariani, C. Giachino, C. Lancini, V. Tosetti, S. Ottolenghi, V. Taylor, S. K. Nicolis, Hippocampal development and neural stem cell maintenance require Sox2-dependent regulation of Shh. *Nat. Neurosci.* **12**, 1248–1256 (2009).

39. J. A. Levy, C. W. LaFlamme, G. Tsaprailis, G. Crynen, D. T. Page, Dyrk1a mutations cause undergrowth of cortical pyramidal neurons via dysregulated growth factor signaling. *Biol. Psychiatry* **90**, 295–306 (2021).

40. L. A. Orosco, A. P. Ross, S. L. Cates, S. E. Scott, D. Wu, J. Sohn, D. Pleasure, S. J. Pleasure, I. E. Adamopoulos, K. S. Zarbalis, Loss of Wdfy3 in mice alters cerebral cortical neurogenesis reflecting aspects of the autism pathology. *Nat. Commun.* **5**, 4692 (2014).

41. S. Hong, J. H. Yi, S. Lee, C.-H. Park, J. H. Ryu, K. S. Shin, S. J. Kang, Defective neurogenesis and schizophrenia-like behavior in PARP-1–deficient mice. *Cell Death Dis.* **10**, 943 (2019).

42. P. Q. Duy, P. Rakic, S. L. Alper, W. E. Butler, C. A. Walsh, N. Sestan, D. H. Geschwind, S. C. Jin, K. T. Kahle, Brain ventricles as windows into brain development and disease. *Neuron* **110**, 12–15 (2022).

43. P. Q. Duy, S. C. Weise, C. Marini, X.-J. Li, D. Liang, P. J. Dahl, S. Ma, A. Spajic, W. Dong, J. Juusola, E. Kiziltug, A. J. Kundishora, S. Koundal, M. Z. Pedram, L. A. Torres-Fernández, K. Händler, E. De Domenico, M. Becker, T. Ulas, S. A. Juranek, E. Cuevas, L. T. Hao, B. Jux, A. M. M. Sousa, F. Liu, S.-K. Kim, M. Li, Y. Yang, Y. Takeo, A. Duque, C. Nelson-Williams, Y. Ha, K. Selvaganesan, S. M. Robert, A. K. Singh, G. Allington, C. G. Furey, A. T. Timberlake, B. C. Reeves, H. Smith, A. Dunbar, T. De Spenza Jr., J. Goto, A. Marlier, A. Moreno-De-Luca, X. Yu, W. E. Butler, B. S. Carter, E. M. R. Lake, R. T. Constable, P. Rakic, H. Lin, E. Deniz, H. Benveniste, N. S. Malvankar, J. I. Estrada-Veras, C. A. Walsh, S. L. Alper, J. L. Schultze, K. Paeschke, A. Doetzlhofer, F. G. Wulczyn, S. C. Jin, R. P. Lifton, N. Sestan, W. Kolanus, K. T. Kahle, Impaired neurogenesis alters brain biomechanics in a neuroprogenitor-based genetic subtype of congenital hydrocephalus. *Nat. Neurosci.* **25**, 458–473 (2022).

44. M. Notaras, A. Lodhi, F. Dündar, P. Collier, N. M. Sayles, H. Tilgner, D. Greening, D. Colak, Schizophrenia is defined by cell-specific neuropathology and multiple neurodevelopmental mechanisms in patient-derived cerebral organoids. *Mol. Psychiatry* **27**, 1416–1434 (2022).

45. F. M. Benes, J. Davidson, E. D. Bird, Quantitative cytoarchitectural studies of the cerebral cortex of schizophrenics. *Arch. Gen. Psychiatry* **43**, 31–35 (1986).

46. F. M. Benes, S. L. Vincent, M. Todtenkopf, The density of pyramidal and nonpyramidal neurons in anterior cingulate cortex of schizophrenic and bipolar subjects. *Biol. Psychiatry* **50**, 395–406 (2001).

47. O. Devinsky, M. J. Morrell, B. A. Vogt, Contributions of anterior cingulate cortex to behaviour. *Brain* **118**, 279–306 (1995).

48. Y. Kim, Y. W. Noh, K. Kim, E. Kim, Hyperactive ACC-MDT pathway suppresses prepulse inhibition in mice. *Schizophr. Bull.* **47**, 31–43 (2021).

49. D. Konno, G. Shioi, A. Shitamukai, A. Mori, H. Kiyonari, T. Miyata, F. Matsuzaki, Neuroepithelial progenitors undergo LGN-dependent planar divisions to maintain self-renewability during mammalian neurogenesis. *Nat. Cell Biol.* **10**, 93–101 (2008).

50. J. D. Godin, K. Colombo, M. Molina-Calavita, G. Keryer, D. Zala, B. C. Charrin, P. Dietrich, M.-L. Volvert, F. Guillemot, I. Dragatsis, Y. Bellaiche, F. Saudou, L. Nguyen, S. Humbert, Huntingtin is required for mitotic spindle orientation and mammalian neurogenesis. *Neuron* **67**, 392–406 (2010).

51. D. Sakai, J. Dixon, M. J. Dixon, P. A. Trainor, Mammalian neurogenesis requires Treacle-Plk1 for precise control of spindle orientation, mitotic progression, and maintenance of neural progenitor cells. *PLOS Genet.* **8**, e1002566 (2012).

52. D. A. Lewis, P. Levitt, Schizophrenia as a disorder of neurodevelopment. *Annu. Rev. Neurosci.* **25**, 409–432 (2002).

53. C. Pantelis, M. Yücel, S. J. Wood, D. Velakoulis, D. Sun, G. Berger, G. W. Stuart, A. Yung, L. Phillips, P. D. McGorry, Structural brain imaging evidence for multiple pathological processes at different stages of brain development in schizophrenia. *Schizophr. Bull.* **31**, 672–696 (2005).

54. X. Zhang, M. H. Chen, X. Wu, A. Kodani, J. Fan, R. Doan, M. Ozawa, J. Ma, N. Yoshida, J. F. Reiter, D. L. Black, P. V. Kharchenko, P. A. Sharp, C. A. Walsh, Cell-type-specific alternative splicing governs cell fate in the developing cerebral cortex. *Cell* **166**, 1147–1162.e15 (2016).

55. L. E. Marasco, A. R. Kornblihtt, The physiology of alternative splicing. *Nat. Rev. Mol. Cell Biol.* **24**, 242–254 (2023).

56. X. Yang, J. Coulombe-Huntington, S. Kang, G. M. Sheynkman, T. Hao, A. Richardson, S. Sun, F. Yang, Y. A. Shen, R. R. Murray, K. Spirohn, B. E. Begg, M. Duran-Frigola, A. M. Williams, S. J. Pevzner, Q. Zhong, S. A. Wanamaker, S. Tam, L. Ghamsari, N. Sahni, S. Yi, M. D. Rodriguez, D. Balcha, G. Tan, M. Costanzo, B. Andrews, C. Boone, X. J. Zhou, K. Salehi-Ashtiani, B. Charloteaux, A. A. Chen, M. A. Calderwood, P. Aloy, F. P. Roth, D. E. Hill, L. M. Iakoucheva, Y. Xia, M. Vidal, Widespread expansion of protein interaction capabilities by alternative splicing. *Cell* **164**, 805–817 (2016).

57. J. S. Cristóvão, V. K. Morris, I. Cardoso, S. S. Leal, J. Martínez, H. M. Botelho, C. Göbl, R. David, K. Kierdorf, M. Alemi, T. Madl, G. Fritz, B. Reif, C. M. Gomes, The neuronal S100B protein is a calcium-tuned suppressor of amyloid-β aggregation. *Sci. Adv.* **4**, eaaq1702 (2018).

58. A. Guemez-Gamboa, N. G. Coufal, J. G. Gleeson, Primary cilia in the developing and mature brain. *Neuron* **82**, 511–521 (2014).

59. T.-Y. Eom, S. B. Han, J. Kim, J. A. Blundon, Y.-D. Wang, J. Yu, K. Anderson, D. B. Kaminski, S. M. Sakurada, S. M. Pruett-Miller, L. Horner, B. Wagner, C. G. Robinson, M. Eicholtz, D. C. Rose, S. S. Zakharenko, Schizophrenia-related microdeletion causes defective ciliary motility and brain ventricle enlargement via microRNA-dependent mechanisms in mice. *Nat. Commun.* **11**, 912 (2020).

60. D. R. Weinberger, Future of days past: Neurodevelopment and schizophrenia. *Schizophr. Bull.* **43**, 1164–1168 (2017).

61. A. E. Jaffe, R. E. Straub, J. H. Shin, R. Tao, Y. Gao, L. Collado-Torres, T. Kam-Thong, H. S. Xi, J. Quan, Q. Chen, C. Colantuoni, W. S. Ulrich, B. J. Maher, A. Deep-Soboslay, B. S. Consortium, A. J. Cross, N. J. Brandon, J. T. Leek, T. M. Hyde, J. E. Kleinman, D. R. Weinberger, Developmental and genetic regulation of the human cortex transcriptome illuminate schizophrenia pathogenesis. *Nat. Neurosci.* **21**, 1117–1125 (2018).

62. A. E. Jaffe, Y. Gao, A. Deep-Soboslay, R. Tao, T. M. Hyde, D. R. Weinberger, J. E. Kleinman, Mapping DNA methylation across development, genotype and schizophrenia in the human frontal cortex. *Nat. Neurosci.* **19**, 40–47 (2016).

63. T. Sawada, T. E. Chater, Y. Sasagawa, M. Yoshimura, N. Fujimori-Tonou, K. Tanaka, K. J. M. Benjamin, A. C. M. Paquola, J. A. Erwin, Y. Goda, I. Nikaido, T. Kato, Developmental excitation-inhibition imbalance underlying psychoses revealed by single-cell analyses of discordant twins-derived cerebral organoids. *Mol. Psychiatry* **25**, 2695–2711 (2020).

64. O. Robicsek, R. Karry, I. Petit, N. Salman-Kesner, F. J. Müller, E. Klein, D. Aberdam, D. Ben-Shachar, Abnormal neuronal differentiation and mitochondrial dysfunction in hair follicle-derived induced pluripotent stem cells of schizophrenia patients. *Mol. Psychiatry* **18**, 1067–1076 (2013).

65. K. Murai, G. Sun, P. Ye, E. Tian, S. Yang, Q. Cui, G. Sun, D. Trinh, O. Sun, T. Hong, Z. Wen, M. Kalkum, A. D. Riggs, H. Song, G.-L. Ming, Y. Shi, The TLX-miR-219 cascade regulates neural stem cell proliferation in neurodevelopment and schizophrenia iPSC model. *Nat. Commun.* **7**, 10965 (2016).

66. H. Kimura, I. Kushima, M. Banno, T. Inada, A. Yoshimi, B. Aleksic, N. Ozaki, Clinical characterization of patients with schizophrenia and 16p13. 11 duplication: A case series. *Neuropsychopharmacol. Rep.* **43**, 267–271 (2023).

67. M. Johnstone, N. A. Vasistha, M. C. Barbu, O. Dando, K. Burr, E. Christopher, S. Glen, C. Robert, R. Fetit, K. G. Macleod, M. R. Livesey, D. S. Clair, D. H. R. Blackwood, K. Millar, N. O. Carragher, G. E. Hardingham, D. J. A. Wyllie, E. C. Johnstone, H. C. Whalley, A. M. McIntosh, S. M. Lawrie, S. Chandran, Reversal of proliferation deficits caused by chromosome 16p13.11 microduplication through targeting NFκB signaling: An integrated study of patient-derived neuronal precursor cells, cerebral organoids and in vivo brain imaging. *Mol. Psychiatry* **24**, 294–311 (2019).

68. S. R. Datta, A. McQuillin, M. Rizig, E. Blaveri, S. Thirumalai, G. Kalsi, J. Lawrence, N. J. Bass, V. Puri, K. Choudhury, J. Pimm, C. Crombie, G. Fraser, N. Walker, D. Curtis, M. Zvelebil, A. Pereira, R. Kandaswamy, D. St. Clair, H. M. D. Gurling, A threonine to isoleucine missense mutation in the pericentriolar material 1 gene is strongly associated with schizophrenia. *Mol. Psychiatry* **15**, 615–628 (2010).

69. X. Ge, C. L. Frank, F. C. de Anda, L.-H. Tsai, Hook3 interacts with PCM1 to regulate pericentriolar material assembly and the timing of neurogenesis. *Neuron* **65**, 191–203 (2010).

70. T. O. Monroe, M. E. Garrett, M. Kousi, R. M. Rodriguiz, S. Moon, Y. Bai, S. C. Brodar, K. L. Soldano, J. Savage, T. F. Hansen, D. M. Muzny, R. A. Gibbs, L. Barak, P. F. Sullivan, A. E. Ashley-Koch, A. Sawa, W. C. Wetsel, T. Werge, N. Katsanis, PCM1 is necessary for focal ciliary integrity and is a candidate for severe schizophrenia. *Nat. Commun.* **11**, 5903 (2020).

71. A. Sumitomo, H. Yukitake, K. Hirai, K. Horike, K. Ueta, Y. Chung, E. Warabi, T. Yanagawa, S. Kitaoka, T. Furuyashiki, S. Narumiya, T. Hirano, M. Niwa, E. Sibille, T. Hikida, T. Sakurai, K. Ishizuka, A. Sawa, T. Tomoda, Ulk2 controls cortical excitatory–inhibitory balance via autophagic regulation of p62 and GABAA receptor trafficking in pyramidal neurons. *Hum. Mol. Genet.* **27**, 3165–3176 (2018).

72. M. Yilmaz, E. Yalcin, J. Presumey, E. Aw, M. Ma, C. W. Whelan, B. Stevens, S. A. McCarroll, M. C. Carroll, Overexpression of schizophrenia susceptibility factor human complement C4A promotes excessive synaptic loss and behavioral changes in mice. *Nat. Neurosci.* **24**, 214–224 (2021).

73. T. Miyakawa, L. M. Leiter, D. J. Gerber, R. R. Gainetdinov, T. D. Sotnikova, H. Zeng, M. G. Caron, S. Tonegawa, Conditional calcineurin knockout mice exhibit multiple abnormal behaviors related to schizophrenia. *Proc. Natl. Acad. Sci. U.S.A.* **100**, 8987–8992 (2003).

74. R. M. Deacon, Assessing nest building in mice. *Nat. Protoc.* **1**, 1117–1119 (2006).

75. B. S. Goo, D. J. Mun, S. Kim, T. T. M. Nhung, S. B. Lee, Y. Woo, S. J. Kim, B. K. Suh, S. J. Park, H.-E. Lee, K. Park, H. Jang, J.-C. Rah, K.-J. Yoon, S. T. Baek, S.-Y. Park, S. K. Park, Schizophrenia-associated mitotic arrest deficient-1 (MAD1) regulates the polarity of migrating neurons in the developing neocortex. *Mol. Psychiatry* **28**, 856–870 (2023).

76. D. Wei, N. Gao, L. Li, J.-X. Zhu, L. Diao, J. Huang, Q.-J. Han, S. Wang, H. Xue, Q. Wang, α-Tubulin acetylation restricts axon overbranching by dampening microtubule plus-end dynamics in neurons. *Cereb. Cortex* **28**, 3332–3346 (2018).

77. H.-J. Shim, J. Lee, S.-G. Kim, BOLD fMRI and hemodynamic responses to somatosensory stimulation in anesthetized mice: Spontaneous breathing vs. mechanical ventilation. *NMR Biomed.* **33**, e4311 (2020).

78. N. Lee, D.-K. Kim, E.-S. Kim, S. J. Park, J.-H. Kwon, J. Shin, S.-M. Park, Y. H. Moon, H. J. Wang, Y. S. Gho, K. Y. Choi, Comparative interactomes of SIRT 6 and SIRT 7: Implication of functional links to aging. *Proteomics* **14**, 1610–1622 (2014).

79. B. Madarampalli, Y. Yuan, D. Liu, K. Lengel, Y. Xu, G. Li, J. Yang, X. Liu, Z. Lu, D. X. Liu, ATF5 connects the pericentriolar materials to the proximal end of the mother centriole. *Cell* **162**, 580–592 (2015).

80. L. Jakobsen, J. M. Schröder, K. M. Larsen, E. Lundberg, J. S. Andersen, "Centrosome isolation and analysis by mass spectrometry-based proteomics" in *Methods in Enzymology* (Elsevier, 2013), vol. 525, pp. 371–393.

81. X. Qian, F. Jacob, M. M. Song, H. N. Nguyen, H. Song, G.-l. Ming, Generation of human brain region–specific organoids using a miniaturized spinning bioreactor. *Nat. Protoc.* **13**, 565–580 (2018).